A&A 642, A227 (2020)
https://doi.org/10.1051/0004-6361/202039032

Astronomy & Astrophysics

The CARMENES search for exoplanets around M dwarfs

Rubidium abundances in nearby cool stars

C. Abia[1], H. M. Tabernero[2,3], S. A. Korotin[4], D. Montes[3], E. Marfil[3], J. A. Caballero[5], O. Straniero[6], N. Prantzos[7], I. Ribas[8,9], A. Reiners[10], A. Quirrenbach[11], P. J. Amado[12], V. J. S. Béjar[13,14], M. Cortés-Contreras[5], S. Dreizler[10], Th. Henning[15], S. V. Jeffers[10], A. Kaminski[11], M. Kürster[15], M. Lafarga[8,9], Á. López-Gallifa[3], J. C. Morales[8,9], E. Nagel[16], V. M. Passegger[17,18], S. Pedraz[19], C. Rodríguez López[12], A. Schweitzer[17], and M. Zechmeister[10]

[1] Departamento de Física Teórica y del Cosmos, Universidad de Granada, 18071 Granada, Spain
e-mail: cabia@ugr.es
[2] Instituto de Astrofísica e Ciências do Espaço, Universidade do Porto, CAUP, Rua das Estrelas, 4150-762 Porto, Portugal
[3] Departamento de Física de la Tierra y Astrofísica & IPARCOS-UCM (Instituto de Física de Partículas y del Cosmos de la UCM), Facultad de Ciencias Físicas, Universidad Complutense de Madrid, 28040 Madrid, Spain
[4] Crimean Astrophysical Observatory, Nauchny 298409, Crimea
[5] Centro de Astrobiología (CSIC-INTA), ESAC, Camino bajo del castillo s/n, 28691 Villanueva de la Cañada, Madrid, Spain
[6] Istituto Nazionale di Astrofisica – Osservatorio Astronomico d'Abruzzo, Via Maggini snc, 64100 Teramo, Italy
[7] Institut d'Astrophysique de Paris, UMR7095 CNRS, Univ. P. & M. Curie, 98bis Bd. Arago, 75104 Paris, France
[8] Institut de Ciències de l'Espai (CSIC-IEEC), Campus UAB, c/ de Can Magrans s/n, 08193 Bellaterra, Barcelona, Spain
[9] Institut d'Estudis Espacials de Catalunya (IEEC), 08034 Barcelona, Spain
[10] Institut für Astrophysik, Georg-August-Universität, Friedrich-Hund-Platz 1, 37077 Göttingen, Germany
[11] Landessternwarte, Zentrum für Astronomie der Universtät Heidelberg, Königstuhl 12, 69117 Heidelberg, Germany
[12] Instituto de Astrofísica de Andalucía (IAA-CSIC), Glorieta de la Astronomía s/n, 18008 Granada, Spain
[13] Instituto de Astrofísica de Canarias, c/ Vía Láctea s/n, 38205 La Laguna, Tenerife, Spain
[14] Departamento de Astrofísica, Universidad de La Laguna, 38206 La Laguna, Tenerife, Spain
[15] Max-Planck-Institut für Astronomie, Königstuhl 17, 69117 Heidelberg, Germany
[16] Thüringer Landessternwarte Tautenburg, Sternwarte 5, 07778 Tautenburg, Germany
[17] Hamburger Sternwarte, Gojenbergsweg 112, 21029 Hamburg, Germany
[18] Homer L. Dodge Department of Physics and Astronomy, University of Oklahoma, 440 West Brooks Street, Norman, OK73019 Oklahoma, USA
[19] Centro Astronómico Hispano-Alemán (CSIC-MPG), Observatorio de Calar Alto, Sierra de los Filabres, 04550 Gérgal, Spain

Received 25 July 2020 / Accepted 20 August 2020

ABSTRACT

Due to their ubiquity and very long main-sequence lifetimes, abundance determinations in M dwarfs provide a powerful and alternative tool to GK dwarfs to study the formation and chemical enrichment history of our Galaxy. In this study, abundances of the neutron-capture elements Rb, Sr, and Zr are derived, for the first time, in a sample of nearby M dwarfs. We focus on stars in the metallicity range $-0.5 \lesssim$ [Fe/H] $\lesssim +0.3$, an interval poorly explored for Rb abundances in previous analyses. To do this we use high-resolution, high-signal-to-noise-ratio, optical and near-infrared spectra of 57 M dwarfs observed with CARMENES. The resulting [Sr/Fe] and [Zr/Fe] ratios for most M dwarfs are almost constant at about the solar value, and are identical to those found in GK dwarfs of the same metallicity. However, for Rb we find systematic underabundances ([Rb/Fe] < 0.0) by a factor two on average. Furthermore, a tendency is found for Rb – but not for other heavy elements (Sr, Zr) – to increase with increasing metallicity such that [Rb/Fe] $\gtrsim 0.0$ is attained at metallicities higher than solar. These are surprising results, never seen for any other heavy element, and are difficult to understand within the formulation of the s- and r-processes, both contributing sources to the Galactic Rb abundance. We discuss the reliability of these findings for Rb in terms of non-LTE (local thermodynamic equilibrium) effects, stellar activity, or an anomalous Rb abundance in the Solar System, but no explanation is found. We then interpret the full observed [Rb/Fe] versus [Fe/H] trend within the framework of theoretical predictions from state-of-the-art chemical evolution models for heavy elements, but a simple interpretation is not found either. In particular, the possible secondary behaviour of the [Rb/Fe] ratio at super-solar metallicities would require a much larger production of Rb than currently predicted in AGB stars through the s-process without overproducing Sr and Zr.

Key words. nuclear reactions, nucleosynthesis, abundances – stars: abundances – stars: late-type

1. Introduction

Analysis of the rubidium abundance in the Solar System shows that the neutron capture s- and r-processes are about equally responsible for the synthesis of this element (e.g. Sneden et al. 2008; Prantzos et al. 2020). Rubidium is present in two isotopic forms: ^{85}Rb, which is stable, and ^{87}Rb, which with a half-life of 5×10^{10} yr may be considered stable from an astrophysical point of view. Astronomical detection of Rb relies on the Rb I lines, which do not permit measurement of the relative isotopic Rb abundances from stellar spectra. The main s-process, which manufactures elements with atomic mass in the range

$90 < A < 209$, is identified with the He-burning shell in low- and intermediate-mass stars (LIMS; $M \lesssim 8\ M_{\odot}$) during the asymptotic giant branch (AGB) phase (e.g. Busso et al. 1999; Käppeler et al. 2011), where neutrons are mainly provided by the $^{13}C(\alpha,n)^{16}O$ reaction. The weak s-process, responsible for a major contribution to the s-process nuclides up to $A \sim 90$, has been recognised as the result of neutron capture synthesis mainly during core He- and shell C-burning phases of massive stars ($M \gtrsim 10\ M_{\odot}$; Arnett & Thielemann 1985; Prantzos et al. 1990; Raiteri et al. 1991; Pignatari et al. 2010; Limongi & Chieffi 2018) with the reaction $^{22}Ne(\alpha,n)^{25}Mg$ being the major neutron source.

The situation concerning the astrophysical site of the r-process is still far from clear. After more than 50 yr of research into its astrophysical origin(s), the identification of a fully convincing site remains elusive. In the recent past, the r-process was usually associated to the explosion of massive stars, but nowadays the neutron-star merging scenario is gaining support, bolstered by the recent joint detection of electromagnetic and gravitational signals from the γ-ray burst GW 170817/GRB 170817A (see Pian et al. 2017, and references therein). Nevertheless, the behaviour of the abundance ratios with respect to Fe of genuine r-process elements, such as Eu, implies that core collapse supernova may also play an important role in r-process nucleosynthesis. In any case, to date, no numerical simulation in the proposed scenarios is able to fully reproduce the observed distribution of the r-process elemental and isotopic abundances in the Solar System. Excellent reviews on this topic can be found in Thielemann et al. (2017), Cowan et al. (2019), and Arnould & Goriely (2020).

There is substantial observational evidence showing that Rb is produced through the main s-process in AGB stars. Abundance analyses of many Galactic and extragalactic AGB stars both of C- and O-rich types show considerable Rb enhancements, namely [Rb/Fe] > 0.0[1] (Lambert et al. 1995; Abia & Wallerstein 1998; Abia et al. 2001; García-Hernández et al. 2006, 2009; de Laverny et al. 2006; Pérez-Mesa et al. 2017). Generally, these enhancements can be explained by the current nucleosynthesis models of AGB stars (Gallino et al. 1998; Cristallo et al. 2011, 2015; van Raai et al. 2012; Karakas & Lattanzio 2014). Two are the possible neutron sources in AGB stars: the $^{13}C(\alpha,n)^{16}O$ reaction, which is the main neutron source in low-mass AGB stars, and the $^{22}Ne(\alpha,n)^{25}Mg$ reaction, which becomes important in massive AGBs. Theoretical models predict [Rb/Sr,Y,Zr] ratios lower or larger than solar depending on whether the $^{13}C(\alpha,n)^{16}O$ or the $^{22}Ne(\alpha,n)^{25}Mg$ reaction is the main neutron source, respectively. The difference is in the neutron density, which is rather low for the $^{13}C(\alpha,n)^{16}O$ reaction ($N_n \sim 10^7$ cm^{-3}), but much larger in the case of the $^{22}Ne(\alpha,n)^{25}Mg$ reaction ($N_n > 10^{11}$ cm^{-3}). Abundance ratios [Rb/Sr,Y,Zr] < 0.0 are indeed found in most carbon-rich AGB stars, which indicates their low-mass AGB origin ($M \sim 1.3$–$3.0\ M_{\odot}$), while positive ratios are found in very luminous O-rich AGB stars with masses $M \gtrsim 4\ M_{\odot}$, in which the ^{22}Ne neutron source is dominant (Lambert et al. 1995; Abia et al. 2001; Pérez-Mesa et al. 2017).

The evolution of the Galaxy's s- and r-process products on the other hand is directly observed from the stellar abundances of elements that are predominantly attributable to either the s- or the r-process (see e.g. Jofré et al. 2019). Traditional tracers include Sr, Ba, and La for the s-process and Eu as the genuine representative element of the r-process[2]. Due to the nearly equal s- and r-process production of Rb, the study of the evolution of the abundance of this element with metallicity is particularly suitable for elucidating the timescales on which both neutron capture processes contribute to the chemical history of the Galaxy. However, the unfavourable electronic structure of Rb provides only a few lines in stellar spectra. The most used lines are the Rb I resonance lines at $\lambda\lambda$7800.3 and 7947.6 Å. Due to the low cosmic abundance of Rb, these lines are usually weak, and in G dwarfs they are also heavily blended. Because of their weakness, the blend issue is aggravated in stars with near solar metallicity (or higher). To date, only two Rb abundance studies in these stars exist, namely those of Gratton & Sneden (1994) and Tomkin & Lambert (1999). These authors derived Rb abundances in a sample of metal-poor disc and halo G dwarfs and concluded that the [Rb/Fe] versus [Fe/H] relationship behaves at low metallicity ([Fe/H] < −1) as does [Eu/Fe], that is, showing an approximately constant [Rb/Fe] ratio as a typical r-process element. However, the behaviour at higher metallicities ([Fe/H] $\gtrsim$ −0.5) is poorly understood. It is precisely at those metallicities that the s-process contribution to the Galactic Rb abundance is expected to peak (e.g. Busso et al. 1999; Cristallo et al. 2015; Bisterzo et al. 2017; Prantzos et al. 2018). Detection via the Rb I resonance lines at the expected low Rb abundances is more favourable for cool dwarfs and giants. Due to the lower effective temperature and higher gravity of M dwarfs, the Rb resonance lines show a moderate intensity in these stars and can be relatively easily identified in their spectra for a wide range of metallicities, in particular in stars with metallicity close to solar using high spectral resolution. However, there is a caveat to using these lines: although prominent, they are contaminated with the presence of a plethora of TiO and VO absorption lines and as a consequence the spectral continuum is usually difficult to locate.

In this study we derive Rb abundances from high-resolution spectra in a sample of nearby, bright, single M dwarfs with metallicities close to solar. Simultaneously, we also determined their Sr and Zr abundances, which are two elements with a predominantly main s-process origin. For that, we use the high signal-to-noise template spectra of 57 M dwarfs observed under the CARMENES exoplanet survey guaranteed time observations (GTOs; Quirrenbach et al. 2018; Reiners et al. 2018). The derived abundance ratios are compared with state-of-the-art chemical evolution model predictions for the solar neighbourhood. Our aim is to better identify the onset of the significant s-process contribution in the chemical history of the Galaxy and put constraints on the role played by the s- and r-processes in the Galactic Rb budget. The structure of this paper is as follows: the observational material and analysis are presented in Sect. 2, where the data acquisition and reduction procedures are briefly described; we also discuss the atmospheric parameters used in this study, the line lists, and the derivation of the abundances from the spectra, together with an evaluation of the observational and analysis uncertainties. In Sect. 3 the main results are discussed and compared with the current nucleosynthesis models through a chemical evolution model for the solar neighbourhood. Finally, Sect. 4 summarises the main conclusions of this study.

[1] Here we follow the standard abundance notation, $[X/H] = \log(X/H)_{\star} - \log(X/H)_{\odot}$, where X/H is the abundance by number of the element X, and $\log \epsilon(X) \equiv \log(X/H) + 12$.

[2] Prantzos et al. (2020) derived an s-process contribution in the Solar System abundances of 91, 88, and 80% for Sr, Ba, and La, respectively, while the r-process contribution for Eu is 95%.

2. Stellar sample and analysis

2.1. Targets, observations, and reduction

Installed at the 3.5 m telescope at Calar Alto Observatory in Almería, Spain, CARMENES is a new-generation spectrograph designed to detect Earth-mass planets around M dwarfs by means of the radial-velocity technique (Quirrenbach et al. 2014, 2018). CARMENES consists of two optical and near-infrared (NIR) channels that extend over 5200–9600 Å in the visual (VIS) and 9600–17 100 Å in the NIR regions with resolving powers of $R = 94,600$ and $R = 80,400$, respectively. The CARMENES exoplanet radial-velocity survey comprises about 350 M dwarfs that cover the full M sequence from M0.0 V to M9.0 V spectral types (and a couple of K7 V stars; Reiners et al. 2018). The CARMENES GTO sample contains a set of carefully selected M dwarfs in the immediate solar neighbourhood that are the brightest stars in each spectral subtype without physical companions at less than 5 arcsec (Caballero et al. 2016a). Most of the target stars should have close to solar composition, although there are some known exceptions (Alonso-Floriano et al. 2015; Passegger et al. 2018, 2019). Almost all the stars studied here are located within a few tens of parsecs around the Sun. However, there are members in all the different Galactic kinematic populations except for the halo, that is, the young thin, thin-to-thick transition, and thick discs (Cortes-Contreras 2016), which ensures a broad investigated metallicity range.

All investigated M dwarfs were spectroscopically observed with CARMENES at a number of epochs since January 2016 (Reiners et al. 2018). The median number of observations per star in the VIS channel is 24. Their spectra were reduced according to the standard CARMENES GTO data flow and thus were processed and wavelength calibrated with the `caracal` pipeline (Caballero et al. 2016b), which computes a single co-added template spectrum per star and instrument channel (see also Zechmeister et al. 2018). The wavelength calibration is provided by a combination of hollow cathode lamps and two temperature- and pressure-stabilised Fabry-Pérot units that eventually provide median uncertainties of the level of 1 m s^{-1} in the VIS channel (Trifonov et al. 2018; Zechmeister et al. 2019), which covers the investigated Rb I, Sr II, and Zr I lines. In addition, we added a step in the data flow, namely correcting the individual spectra from telluric correction before merging them in the template spectra. This correction provided a further improvement in the S/N of the eventually used spectra, up to about 300. Further details on the removal of the telluric features can be found in Nagel et al. (2020).

We selected a sample of 57 M dwarfs from the CARMENES GTO programme in a wide metallicity range ($-0.5 \leq$ [Fe/H] $\leq +0.3$), imposing $T_{\rm eff} > 3400$ K to minimise the impact of molecular absorption, according to the values reported by Passegger et al. (2019). This metallicity interval was poorly explored for Rb abundances in the literature.

2.2. Stellar parameter refinement

A number of studies focused on improving the precision of M dwarf stellar parameters, namely $T_{\rm eff}$, surface gravity ($\log g$), and metallicity, can be found in the recent literature. For instance, different ways to determine the first two parameters were discussed by Veyette et al. (2017), Schweitzer et al. (2019), and Souto et al. (2020), while Birky et al. (2020) discussed the derivation of the metallicity. In contrast to FGK dwarfs, the spectroscopic method to derive these parameters is, in general, not recommended for M dwarfs because of their much more complex spectra. Due to their relatively low effective temperatures ($T_{\rm eff} \lesssim 4000$ K), the spectra of M dwarfs show a plethora of molecular absorption lines that leave almost no atomic line free of blends. Furthermore, the C/O ratio is revealed as an additional relevant parameter in the analysis. The envelopes of M dwarfs are not expected to be affected by the nuclear burning in the stellar interior, and therefore they should show a C/O identical to that of the interstellar medium (ISM) from which they were born, that is, lower than unity. This means that almost all the available carbon in the atmospheres of M dwarfs will be locked into forming CO, while the remaining available oxygen would form metallic oxides, water, and other, less abundant O-bearing molecules. In fact, the VIS spectra of M dwarfs are dominated by TiO and VO absorption bands (and some CaH; Kirkpatrick et al. 1991; Alonso-Floriano et al. 2015), whereas CO, OH, and H_2O prevail in the NIR region. Therefore, to determine the stellar parameters of M dwarfs, a full spectral synthesis analysis is recommended instead of studying individual spectral lines. To do this, an estimation of C/O is vital as the intensity of the above-mentioned O-bearing molecules mainly depends on this ratio. As a consequence, this combined molecular absorption systematically depresses the spectral continuum, which is usually not well defined (e.g. Tsuji & Nakajima 2014).

In a first step we adopted the stellar parameters derived by Passegger et al. (2019), who fitted an updated version grid of the PHOENIX synthetic spectra presented by Husser et al. (2013) to the selected high-resolution CARMENES spectra in the VIS and NIR spectral ranges using a χ^2 method. We refer to their work for further details on the specific method followed, for a detailed discussion on the evaluation of the uncertainties, and for comparison with the most recent literature. In general, the agreement with other studies was good within the uncertainties, although for some stars with metallicity higher than solar, Passegger et al. (2019) derived systematically higher metallicities.

With the stellar parameters estimated as mentioned above, a model atmosphere was interpolated within the grid of MARCS atmosphere models (Gustafsson et al. 2008) for the specific $T_{\rm eff}$, $\log g$, and [M/H] (i.e. average metallicity) derived for each star. A microturbulence parameter of $\xi = 1$ km s^{-1} was adopted for all the stars. Certainly, other microturbulence parameters might be possible for M dwarfs, but the severe blending prevented us for deriving this parameter spectroscopically. However, uncertainties of 0.5 km s^{-1} in the microturbulent velocity result in very small changes in the derived abundances (see below). The atomic line lists were taken from the VALD3 database adopting the corrections performed within the *Gaia*-ESO survey (Heiter et al. 2015) in the VIS wavelength range, while in the NIR range we used the atomic line list from the APOGEE survey (Hasselquist et al. 2016; Cunha et al. 2017; Majewski et al. 2017; Smith et al., in prep.). We refer to these surveys for a detailed description of these line lists. Molecular line lists were provided by B. Plez[3] and they include several C- and O-bearing molecules (CO, CH, CN, C_2, HCN, TiO, VO, H_2O) and a few metallic hydrides (FeH, MgH, CaH). TiO and H_2O determine, in particular, the continuum level at VIS and NIR wavelengths, respectively.

Oscillator strengths for the Rb I resonance lines at $\lambda\lambda$7800 and 7947 Å are known with good accuracy (Morton 2000), but they have multiple components due to the hyperfine structure of the atomic levels. The individual hyperfine structure components

[3] These molecular line lists are publicly available at `https://nextcloud.lupm.in2p3.fr/s/r8pXijD39YLzw5T`, where detailed bibliographic sources can be also found.

Table 1. Spectroscopic data of the used lines and hyperfine structure of Rb I.

Element/ isotope	λ (Å)	$\log gf$
^{87}Rb		
	7800.183	–0.663
	7800.186	–0.663
	7800.188	–1.061
	7800.317	–0.216
	7800.322	–0.663
	7800.325	–1.362
	7947.507	–0.669
	7947.524	–1.368
	7947.651	–0.669
	7947.668	–0.669
^{85}Rb		
	7800.233	–0.744
	7800.234	–0.647
	7800.235	–0.760
	7800.292	–0.282
	7800.295	–0.647
	7800.296	–1.191
	7947.563	–0.653
	7947.570	–1.197
	7947.626	–0.750
	7947.634	–0.653
Sr II		
	10327.311	–0.353
Zr I		
	8063.090	–1.620
	8070.080	–0.790

and their respective oscillator strengths are given in Table 1. We adopted the meteoritic ^{85}Rb/^{87}Rb = 2.43 ratio (Lodders 2019). Unfortunately, the isotopic splitting is tiny and does not allow the derivation of the ^{85}Rb/^{87}Rb ratio from our spectra. Concerning Sr, this element has only a few lines useful for abundance determinations. In fact, the available strontium lines (usually Sr II) in the blue spectral region of cool stars with near-solar metallicity are usually strongly blended. An alternative are the three Sr II lines in the NIR at $\lambda\lambda$10036, 10 327, and 10 914 Å, which are almost free of blends and telluric contamination. However, as shown in Belyakova & Mashonkina (1997), Andrievsky et al. (2011), and Bergemann et al. (2012), these lines are instead strongly affected by deviations from local thermodynamical equilibrium (LTE; see below). Of these Sr lines, we could use only that at λ10 327 Å because that at λ10 036 Å is very weak and blended and located at the edge of one of the CARMENES orders, and the other, at λ10 914 Å, is in one of the spectral gaps of the instrument[4]. For the 10 327 Å line, we used the oscillator strength given by Warner (1968) and the Van der Waals parameters provided by the Anstee, Barklem, and O'Mara theory (see Barklem et al. 2000). This Sr II λ10327 Å line is apparently free of atomic and molecular blends in our stars. In fact, in this spectral region the true spectral continuum can be placed more easily. Finally, the only useful zirconium lines detected in our spectra are the Zr I lines at $\lambda\lambda$8063.105 and 8070.115 Å. These lines are rather weak but not particularly affected by TiO blends in our stars. Oscillator strengths for these lines were taken directly from the VALD3 database. Unfortunately, no yttrium line useful for abundance analysis was detected in the available spectral range.

2.3. Spectral synthesis

We firstly tested our line list by fitting the observed spectra of the Sun and Arcturus (Reiners et al. 2016; Hinkle et al. 1995) in the spectral ranges of interest. In these stars, the Rb I λ7800 Å line is heavily blended with a Si I line, for which we adopted $\log gf = -0.75$ from VALD3. Synthetic spectra in LTE were computed with the corresponding model atmosphere using the code `Turbospectrum v19.1`[5] (Plez 2012). For the Sun, we used a MARCS atmosphere model with parameters $T_{\rm eff}/\log g/\xi = 5770/4.44/1.1$, and for Arcturus a model atmosphere with parameters according to Ryde et al. (2009). Theoretical spectra were convolved with a Gaussian kernel according to the resolving power of the observed spectra and to mimic the macroturbulence parameter. For the Sun, we obtained an LTE Rb abundance of $\log\epsilon$(Rb) = 2.47 ± 0.05 (average value of the two lines). This nicely agrees with the value derived by Grevesse et al. (2015). For Arcturus, the Rb abundance derived was 2.01 ± 0.01, which is also in very good agreement with the abundance obtained by Tomkin & Lambert (1999) and Yong et al. (2006) of namely 2.02 ± 0.02. A similar test was made for Zr from the selected Zr I lines. Also, nice agreement in the abundance of Zr was found with the values derived by Grevesse et al. (2015) and Peterson et al. (1993) in the Sun and Arcturus, respectively, within 0.05 dex. In the case of Sr, the LTE abundance derived from the Sr II λ10327 Å is significantly larger than that usually accepted in the Sun and Arcturus, suggesting deviations from LTE in the formation of this line. Eventually, we adopted the solar LTE abundances recommended by Lodders (2019) for Rb (2.47) and Zr (2.58) which nicely agree with the values obtained here (for Sr, see below). We also used the solar photospheric abundances recommended by this author for the rest of the elements.

The spectral synthesis method for abundance analysis should be applied preferentially when the true continuum can be defined. For this reason, it may be difficult to apply to M dwarfs, for which the true continuum cannot be defined in general. In these stars, the presence of strong TiO absorption and a veil of numerous weak lines of H_2O in the VIS and NIR spectral ranges, respectively, depress the continuum level by some parts per hundred. However, in our case an upper envelope of the spectrum can be well defined by connecting the highest flux points in the spectrum in all the stars. This pseudo-continuum can then be relocated with the help of the synthetic spectrum itself. To place this pseudo-continuum, the estimation of C/O is critical, because this ratio determines the intensity of TiO and H_2O lines for a given set of stellar parameters. We followed the iterative method described below.

(a) First, a synthetic spectrum was computed for each star with the carbon and oxygen abundances scaled to the metallicity of the model atmosphere (see above and Passegger et al. 2019). However, for the star J13450+176 (BD+18 2776; [M/H] = −0.5), we considered an oxygen enhancement in the model atmosphere, namely, [O/Fe] = +0.4, a value typically found in G dwarfs of similar metallicity. We always kept the C abundance constant. Unfortunately, the CO and CN lines in the covered spectral ranges are too weak to determine the C abundance. Nevertheless, we checked that variations of the

[4] https://carmenes.caha.es/ext/instrument/

[5] https://github.com/bertrandplez/Turbospectrum2019/

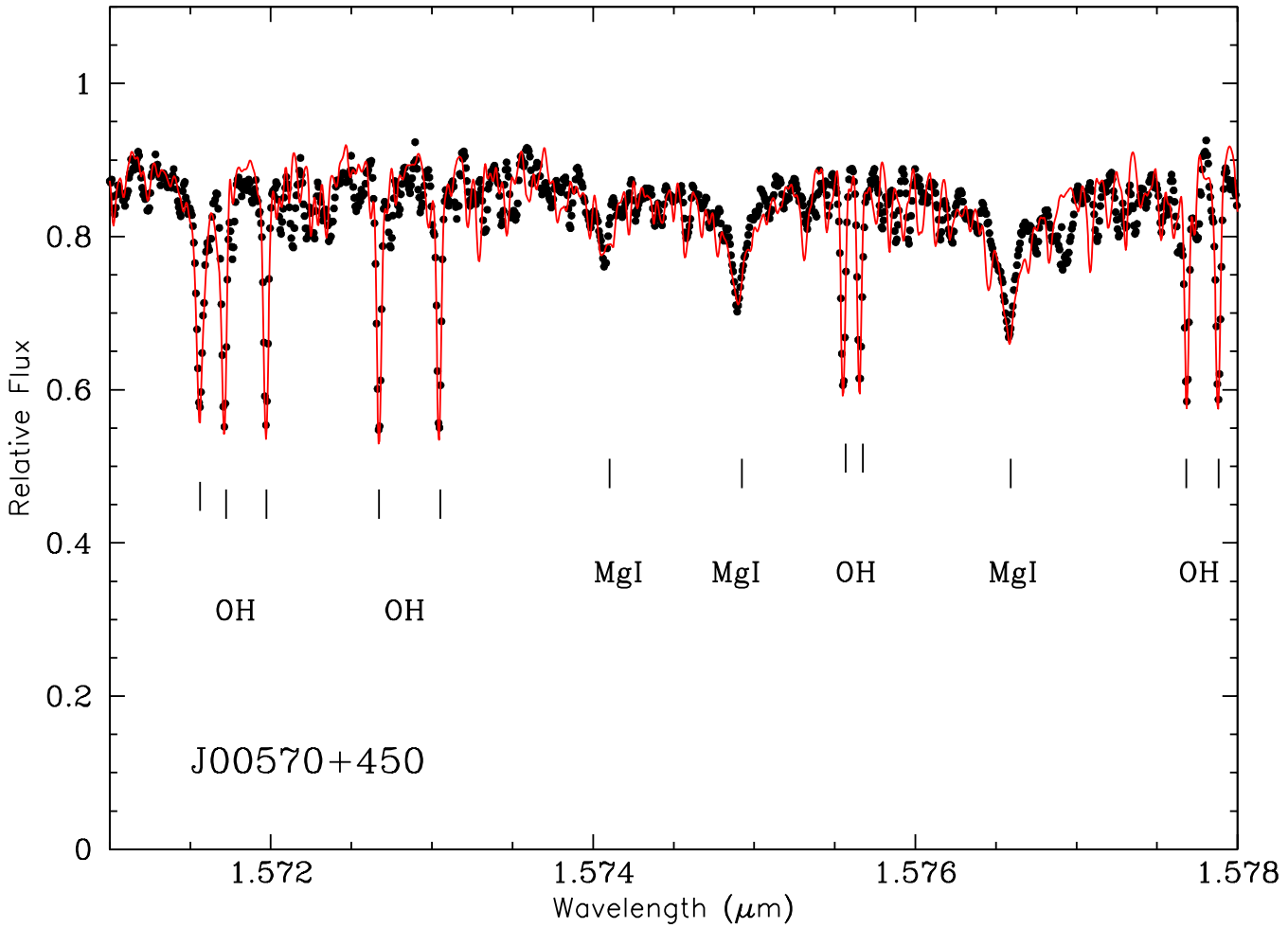

Fig. 1. Comparison of the observed (black dots) and synthetic (solid red line) spectra for the M3.0 V star J00570+450 (G 172–30) in the spectral region around $\lambda\lambda$15 750 Å. Some OH lines, from which the O abundance was derived, and less intense Mg I lines near $\lambda\lambda\lambda$15740, 15749, and 15765 Å are marked and labelled. In this region the pseudo-continuum is reduced mainly due to the contribution of an H_2O veil.

C abundance (within ∼0.25 dex) have almost no effect on the synthetic spectrum in the spectral ranges of interest. To compute this initial theoretical spectrum, we did not include the atomic and OH lines in the synthesis. In a similar way, theoretical spectra were convolved with a Gaussian function according to the spectral resolution and to mimic the macroturbulence parameter. The stars Karmn J11201–104 (LP 733–099) and J15218+209 (OT Ser), which show broader lines, were left out of this convolution. For these stars, the observed spectrum was better fitted with a rotational profile. Indeed, Reiners et al. (2018) quoted $v \sin i > 2\,\mathrm{km\,s^{-1}}$ for these stars. For them, we used a rotational profile with FWMH in the range 4–6 $\mathrm{km\,s^{-1}}$. The profiles of the Rb lines in these stars and in J18174+483 (TYC 3529–1437–1) may also be affected by the magnetic field (see below).

(b) We then compared the location of the pseudo-continuum in the NIR region with that inferred from the theoretical spectrum itself (mainly determined by the H_2O veil). In general, corrections smaller than about 3% were needed. We then included the atomic and OH lines in the synthesis and estimated the O abundance by fitting selected OH lines, in particular those in the region between 1.57 and 1.59 μm (see Fig. 1). The O abundance derived from these selected OH lines should be compatible with the metallicity obtained from the nearby metallic lines (within its uncertainty of ±0.19 dex according to Passegger et al. 2019; see Fig. 1)[6]. This agreement also served as an additional test for the reliability of the pseudo-continuum location.

(c) With the O abundance derived in this way, we then compared the observed and calculated intensity of TiO bands in the VIS region, in particular the band at $\lambda > 7000$ Å. Adjustments to the O abundance adopted in the synthetic spectrum were made when needed; in any case, they never exceed ∼0.20 dex.

(d) Finally, with this new O abundance, we fitted again the OH lines in the NIR region and repeated the procedure until we achieved convergence (within ∼0.1 dex) between the O abundances estimated from both spectral ranges. Table A.1 shows the final C/O derived in our stars. As expected, most of them are very close to the solar ratio (0.575, according to Lodders 2019), but a few stars show significantly lower C/O or higher than this value.

Once the C/O ratio was determined, the next step in the analysis was the determination of the stellar metallicity in a more accurate way. As mentioned above, the initial metallicitiy was taken from Passegger et al. (2019). However, these metallicities were derived from metallic lines that have moderate (or large) intensity in the atmospheres of M dwarfs and therefore might be affected by saturation effects. A better determination of the metallicity was therefore desirable. To do

[6] For unevolved, near-solar metallicity stars, [O/Fe] ≈ 0.0.

that, we used a number of weak metallic lines available in the spectral range close to the Rb, Sr, and Zr lines. The specific lines were the Ca I line at λ10 343.819 Å; the Ti I lines at $\lambda\lambda$ 7791.349, 7949.152, 8068.239, and 8069.799 Å; the Fe I lines at $\lambda\lambda$7802.473, 7941.088, 7945.846, and 10 340.885 Å; and the Ni I lines at $\lambda\lambda$7788.930 and 7797.580 Å. The weakness of these lines (except that of Ca I) should minimise saturation effects and possible deviations from LTE. In addition, their proximity to the heavy element (Rb, Sr, and Zr) lines may reduce systematic effects introduced by the uncertain location of the pseudo-continuum when deriving the elemental ratios with respect to the average metallicity ([X/M]), since this uncertainty should cancel out. Figures 2 and 3 show synthetic fits to some of these metallic lines. In most of the stars we found good agreement between the metallicity derived from these metallic species, with a dispersion of about ±0.1 dex. Also, in general our metallicities agree within the uncertainty with those derived by Passegger et al. (2019), initially adopted here. Nevertheless, when a difference larger than 0.15 dex was found, we recalculated a model atmosphere with the new metallicity and repeated the derivation of the metallicity until convergence was reached. The largest differences with respect to the metallicities by Passegger et al. (2019) are found in stars with super-solar metalliciy ([M/H] > 0.0). For these stars, we found systematically lower metallicities. This difference may be due, as mentioned above, to the fact that in metal-rich stars the lines selected by these latter authors are very strong and possibly more affected by saturation effects. Systematic differences in metallicity are found between Passegger et al. (2019) and similar studies in M dwarfs, although they could also be related to differences in the stellar parameters (see the discussion in Passegger et al. 2019 for details). Table A.1 shows the final average metallicity ([M/H]) derived for our stars. The overwhelming majority have metallicity close to solar except for the star J13450+176 (BD+18 2776), which is a mildly metal-poor star. This classification agrees with the metallicity determined by other studies for this star (e.g. Gaidos et al. 2014; Mann et al. 2015). Since for near-solar metallicity stars, it holds that [Ni/Fe] ≈ [Ti/Fe] ≈ [Ca/Fe] ≈ 0.0, in the following we refer indistinctly to [M/H] or [Fe/H] as the stellar metallicity.

Once C/O and metallicity were determined, the abundances of Rb, Sr, and Zr were also determined by spectral synthesis fits to the corresponding spectral features. Figure 2 shows an example of a theoretical fit (red lines) to the spectral regions of the Rb lines in a representative star of the sample. The depression of the continuum mainly due to TiO is particularly apparent in the region of the Rb I λ7800 Å line. Fits to some of the metallic lines used for the determination of the average metallicity are also shown. Similarly, Fig. 3 shows fits to the Zr I λ8070 Å (left panel) and Sr II λ10 327 Å (right panel) lines, respectively. The spectral region of the strontium line is apparently not affected by the veil of molecular absorption and therefore the real continuum can be more easily traced.

The two main sources of error in the abundances are measurement and analysis error caused by errors in the adopted model atmosphere parameters. The scatter of the abundances provided by individual lines of the same species is a good guide to measurement error. We found excellent agreement between the Rb abundances derived from both lines, with a dispersion of less than 0.05 dex (see Table A.1). This agreement contrasts with the differences (∼0.1 dex) found by Tomkin & Lambert (1999) and Yong et al. (2006), which led them to exclude the Rb I λ7947 Å line from their analyses, which appeared to be more highly blended. For zirconium, we also found excellent agreement between the abundances derived from both lines (see again Table A.1). The error caused by uncertainties in the adopted stellar parameters can be estimated by modifying the stellar parameters by the quoted errors in the analysis of a typical star in the sample and checking the effect on the abundance derived for each species, namely: ±60 K in $T_{\rm eff}$, ±0.06 dex in $\log g$, ±0.5 km s^{-1} in ξ, ±5% in C/O, and ±0.15 dex in [Fe/H]. For a typical M dwarf with parameters $T_{\rm eff}/\log g/$[Fe/H] = 3750/4.7/0.0, we found that the abundances derived are mostly affected by the uncertainty in $T_{\rm eff}$: ±0.10, ±0.10, and ±0.08 dex for Rb, Sr, and Zr, respectively. The uncertainties in gravity and microturbulence have a similar, although minimal impact on the abundances derived for the three elements (≤0.03 dex). The uncertainty in the metallicity and C/O has a slightly larger effect and is typically 0.05 dex for the three species. Adding these uncertainties together quadratically with the dispersion around the mean abundance value and the continuum uncertainty (about 1–2% in the case of Rb and Zr), we estimated a total uncertainty in [X/H] of ±0.12 dex for Rb and Sr, and ±0.10 dex for Zr. For these heavy elements, the abundance of the element relative to average metallicity, [X/Fe], holds the most interest. This ratio is more or less sensitive to the uncertainties in the atmospheric parameters depending on whether changes in the stellar parameters affect the heavy element abundance and metallicity in the same or opposite sense. In our case, we estimated total uncertainties of ±0.12, ±0.14, and ±0.13 dex for [Rb/Fe], [Sr/Fe], and [Zr/Fe], respectively.

2.4. Non-LTE effects in Rb I and Sr II lines

It is well known that the resonant lines of other alkali elements, such as Na or K, are strongly influenced by deviations from LTE (Bruls et al. 1992). The structure of the energy levels of Rb I is very similar to those of K I and Na I and, by analogy, some non-LTE effects in the formation of Rb lines are expected. As far as we know, no previous study exists on non-LTE effects in Rb I in the literature. Below we briefly describe the method followed to evaluate these effects in M dwarfs. A detailed discussion in a wider range of stellar parameters will be presented elsewhere (Korotin 2020).

Our rubidium atom model includes 29 levels of Rb I and the ground level of Rb II. Radiative transitions between higher levels are very weak and should not affect the accuracy of the non-LTE calculation. Fine structure was considered only for the 5p $2P^0$ level, since it is closely connected to the most important transitions including the resonance lines. In the atmospheres of cool dwarfs, Rb exists almost exclusively in the form of Rb II, since its first ionisation potential is only 4.18 eV. In turn, all excited Rb II levels are separated from the main one by more than 16.5 eV. Nevertheless, 180 supplementary levels of Rb I and 15 levels of Rb II were included in the model to assure the conservation of the particle number. In total, 160 radiative transitions were taken into account for the calculation of the population levels. We included collisional transition rates between the first six levels of Rb I according to Vainshtein et al. (1979). For other collisional transitions between levels with energies below 3.9 eV, calculations from Park (1971) were used. For the rest of the bound–bound collisional transitions, we adopted the formulae from van Regemorter (1962) for permitted transitions and from Allen (1973) for the forbidden ones. Collisional ionisation rates were calculated using the formula from Seaton (1962). Collisions with hydrogen for the first nine levels were described using the detailed quantum mechanical calculations from Yakovleva et al. (2018). For other levels, the classical Drawin formula was used

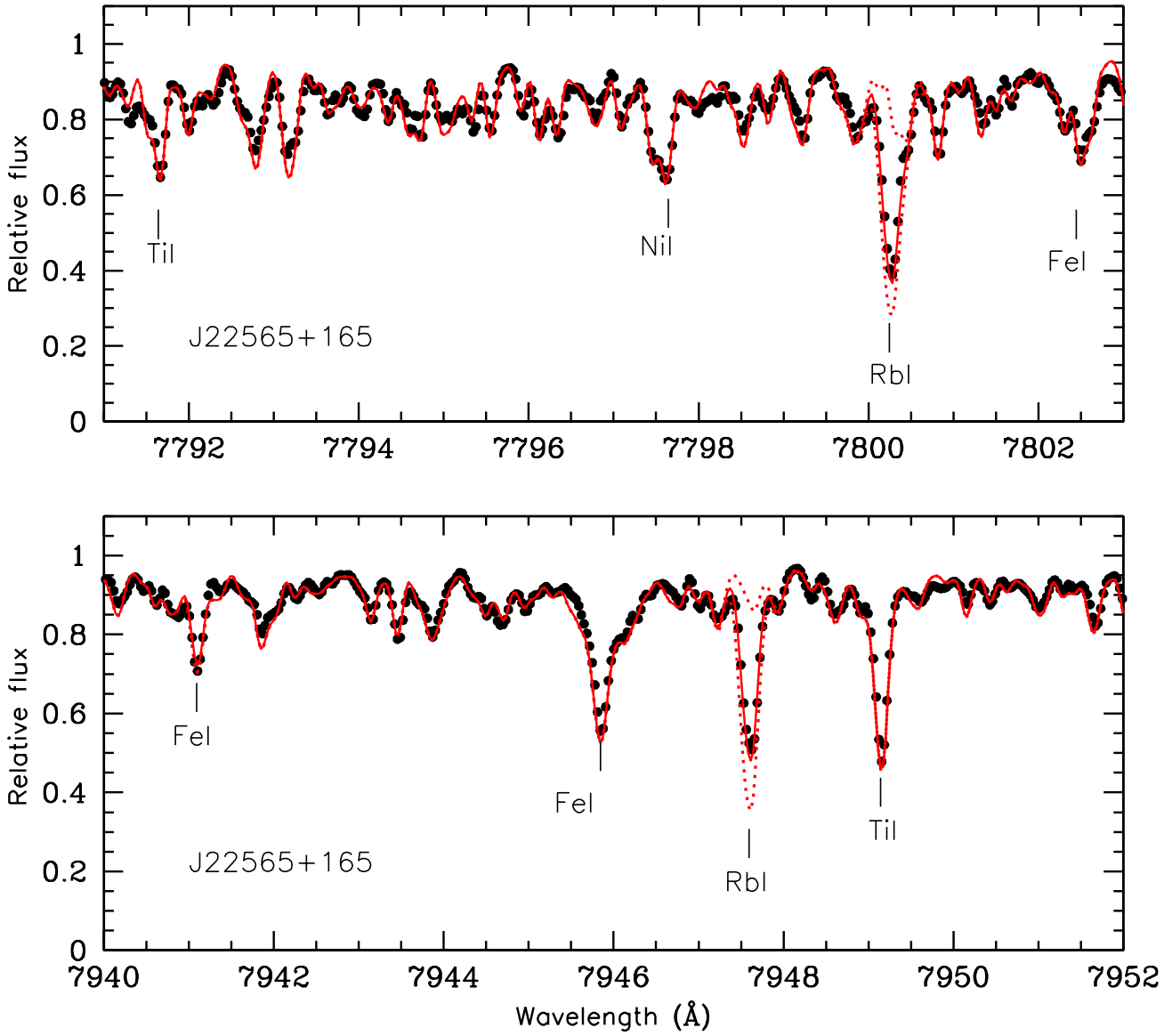

Fig. 2. Same as Fig. 1 but for the regions around Rb I λ7800 Å (*top panel*) and Rb I λ7947 Å (*bottom panel*) for the M1.5 V star J22565+165 (HD 216899). Red solid, and dotted curves show theoretical spectra computed with $\log \epsilon$(Rb) = 2.8, 2.55 (best fit), and no Rb, respectively. Some Ti I, Ni I, and Fe I lines are marked and labelled. In these regions, the pseudo-continuum is reduced mainly due to the contribution of TiO.

in the form suggested by Steenbock & Holweger (1984) with the correction factor $S_H = 0.05$. The population of the atomic levels for Rb I was determined using the code MULTI (Carlsson 1986) with some modifications following Korotin et al. (1999).

The non-LTE corrections lead to a strengthening of the resonance lines in cool dwarfs ($\log g > 4.0$). This strengthening is due to the overpopulation of the ground level because of the so-called super-recombination processes. These processes are common in other alkali metals and were described in detail in Bruls et al. (1992). We first tested our non-LTE calculations for the Rb lines with the Sun. The correction was −0.12 dex, and we obtained a solar non-LTE abundance of Rb of 2.35 ± 0.05. It is noteworthy that this value is, for the first time, in very good agreement with the recommended meteoritic abundance (2.36 ± 0.03, Lodders 2019). We then calculated a grid of non-LTE corrections for the stellar parameters typical of our stellar sample, namely $T_{\rm eff}$ from 3500 to 4500 K, $\log g$ from 4.0 to 5.0 dex, [Fe/H] from −0.5 to +0.5 dex, and [Rb/H] from −0.4 to +0.4 dex (see Table A.1). In general, the non-LTE correction decreases with increasing temperature since the hydrogen collisions become more important. The value of the correction is also determined by changes in the distribution of the average intensity with wavelength and depth in the stellar atmosphere, also affecting the efficacy of the super-recombination processes. However, the fraction of Rb I below ∼4500 K increases and the intensity of the resonance lines increases sharply. The resonance lines are formed mainly in the highest layers of the photosphere where the density is the lowest and the collision rates cannot compensate the imbalance introduced by radiative processes, and therefore the non-LTE correction increases. This effect is enhanced with increasing [Rb/Fe] ratio (see Fig. 4). Non-LTE abundance corrections range from −0.25 to −0.03 dex, being ∼−0.15 dex on average for the typical atmosphere parameters of our stars. Figure 4 shows an example of the non-LTE abundance corrections to the Rb I λ7800 Å line for specific atmosphere parameters and derived [Rb/Fe] ratios. As expected, the

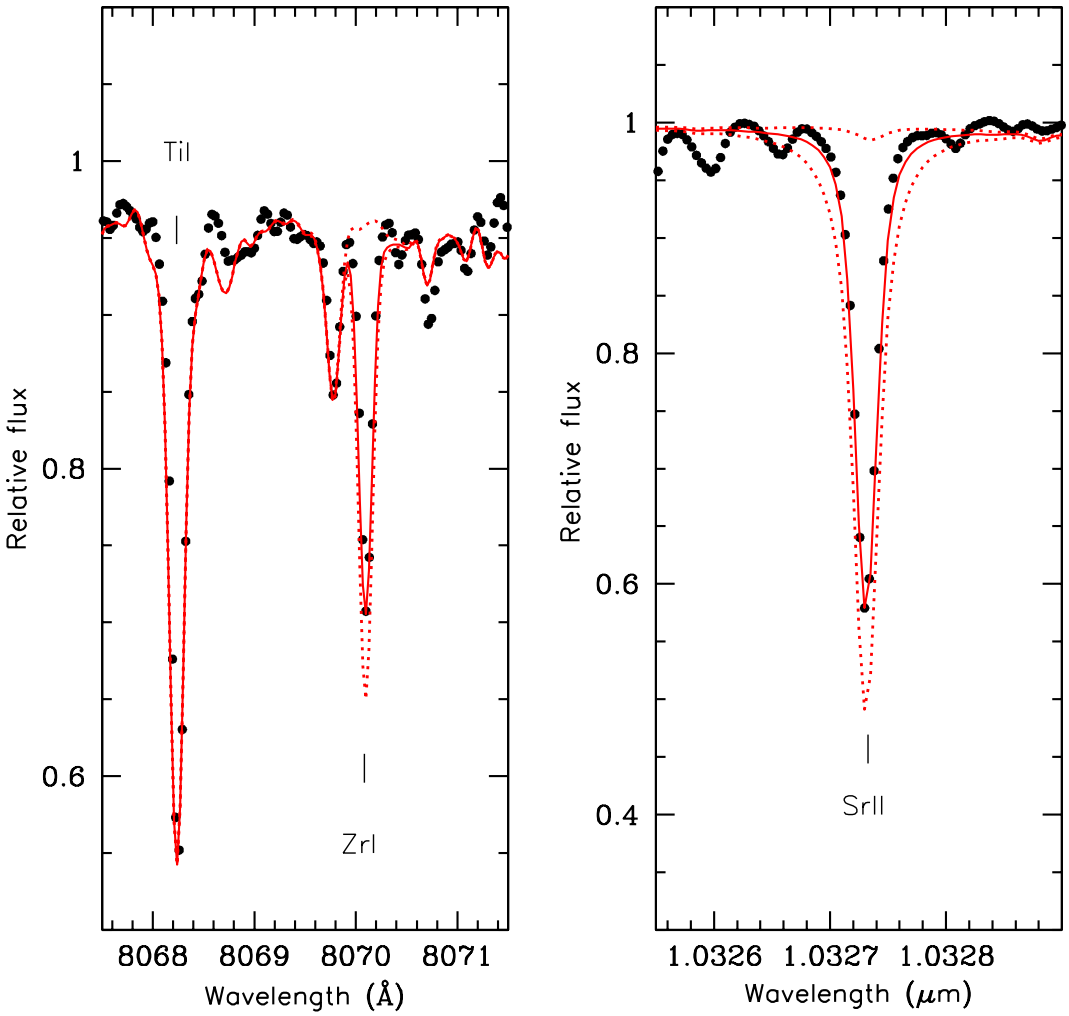

Fig. 3. Same as Fig. 1 but for the spectral regions of Zr I λ8070 Å (*left panel*) and Sr I λ10 327 Å (*right panel*) for the same star. Red solid, and dotted curves show theoretical spectra computed with $\log\epsilon(\mathrm{Zr}) = 3.0$, 2.75 (best fit), and no Zr, respectively, in the *left panel* and with $\log\epsilon(\mathrm{Sr}) = 3.5$, 3.2 (best fit in LTE), and no Sr, respectively, in the *right panel*.

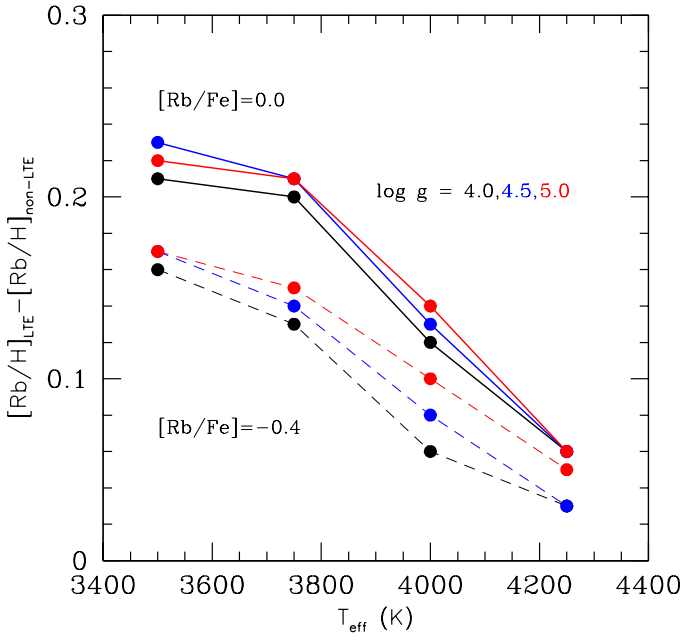

Fig. 4. Difference between the LTE and non-LTE Rb abundances derived from the Rb I λ7800 Å line for typical $T_{\rm eff}$ and $\log g$ (colour coded) in our sample stars. Solid and dashed lines correspond to [Rb/Fe] ratios of 0.0 and −0.4, respectively (see text for details).

non-LTE correction decreases with increasing $T_{\rm eff}$ and decreasing $\log g$. However, for the Rb I λ7947 Å line, corrections are slightly lower for a given set of atmosphere parameters and Rb abundance because this line forms slightly deeper in the atmosphere. Again, a more detailed discussion will be presented in Korotin (2020) including non-LTE corrections in giant stars. In passing, we note that our non-LTE correction for Rb in Arcturus is almost zero.

To evaluate the non-LTE effects in the formation of the Sr II line in the NIR, we used the atom model proposed by Andrievsky et al. (2011). We refer to this author for a more detailed description of the atomic levels used and non-LTE calculations. Briefly, collisional transitions caused by inelastic collisions with H I were considered according to the formulae of Drawin (1968) as compiled by Steenbock & Holweger (1984) with a correction factor of $S_H = 0.01$. This correction factor was obtained by fitting the line profile of different multiplets in the solar spectrum, and was confirmed by the analysis of Bergemann et al. (2012). Atomic level populations were also determined using the code MULTI with modifications according to Korotin et al. (1999). The atomic model used here describes correctly the profiles of the Sr lines in the blue and NIR spectrum of the Sun, giving an identical Sr abundance (2.92; this is the value adopted in this study as the solar Sr abundance). For Arcturus, the non-LTE analysis gave a very similar Sr abundance, namely 2.23 ± 0.04 dex from the three NIR lines, which is significantly

lower than the LTE value of 2.40 from Peterson et al. (1993). It should be noted that non-LTE effects in Sr lines differ significantly from line to line. For instance, in the spectrum of the Sun the resonance lines ($\lambda\lambda$4077.71 and 4215.52 Å) form almost in LTE, the two subordinate blue lines ($\lambda\lambda$4161.79 and 4305.44 Å) show weak non-LTE corrections (∼+0.05 dex), while for the NIR lines non-LTE corrections are severe (from −0.20 to −0.36 dex). Unfortunately, of these three lines, only that at λ10 327 Å is covered by CARMENES. Similarly to Rb, we calculated a grid of non-LTE abundance corrections within the range of the atmospheric parameters of our stars and Sr abundances in the range $-0.3 \leq$ [Sr/H] $\leq +0.3$. Non-LTE abundance corrections are also negative and range from −0.28 to −0.13 dex, with the correction decreasing with increasing temperature and gravity. The correction is larger for moderately metal-poor stars due to the smaller contribution of collisions in the statistical equilibrium. The non-LTE abundances of Sr derived are shown in Table A.1 (we prefer not to include the non-LTE Rb abundances in this table for succinctness). The effect is Rb abundances typically lower by ∼0.15 dex.

3. Results and discussion

Table A.1 shows the Rb, Sr, and Zr abundances determined in our sample of stars. As is customary, the abundances in Table A.1 are plotted as [X/Fe] against [Fe/H] in Fig. 5 to reveal trends in the relative abundance of element X and the metallicity. Two points are immediately apparent:

(1) The [Sr,Zr/Fe] ratios derived in M dwarfs (blue dots) nicely agree with those derived in FGK dwarfs (grey dots) for the metallicity range studied here. Data in FGK dwarf stars were taken from Battistini & Bensby (2016), Delgado Mena et al. (2017), and Mishenina et al. (2019), which we considered as representative studies in the recent literature based on very high S/N spectra (formal errors in [Fe/H] and [Sr,Zr/Fe] in these studies were typically 0.06 dex and ∼0.10 dex, respectively). For the range of metallicity studied, the [Sr/Fe] ratio clusters around the solar value, the average ratio being -0.06 ± 0.10 dex. The [Zr/Fe] ratio shows a small trend of increasing ratio for decreasing metallicity, identical to that found in FGK dwarfs (grey dots), although observations indicated that this trend flattens in metal-poor stars ([Fe/H] < −1.5, see e.g. Brewer & Carney 2006; Reddy et al. 2006)[7]. For [Zr/Fe] the average ratio is 0.06 ± 0.09 dex. In both cases (Sr and Zr), the dispersion around the mean is lower than the expected observational errors in the [X/Fe] ratios.

(2) The [Rb/Fe] ratios derived in M dwarfs are systematically below the solar value. This deficiency is on average [Rb/Fe] = -0.26 ± 0.13 dex in the metallicity range studied, and would remain if non-LTE Rb abundances were used instead because the systematic correction by ∼0.15 dex to lower abundances would be almost compensated by a lower solar Rb abundance (2.35; see above) when deriving the [Rb/Fe] ratio. Interestingly, Fig. 5 (top panel) shows that the few [Rb/Fe] ratios derived in FGK dwarfs in the similar metallicity range also show negative values. This behaviour is in contrast with that of its associated elements Sr and Zr. However, the average [Rb/Fe] ratio shows a significant dispersion, slightly larger than the expected observational errors. Furthermore, a hint of an increasing trend in the [Rb/Fe] ratio with metallicity can be seen for [Fe/H] $\gtrsim -0.3$, although this trend is weak (correlation coefficient of $r = 0.43$).

[7] It is beyond the scope of this study to discuss the abundance trends in metal-poor stars.

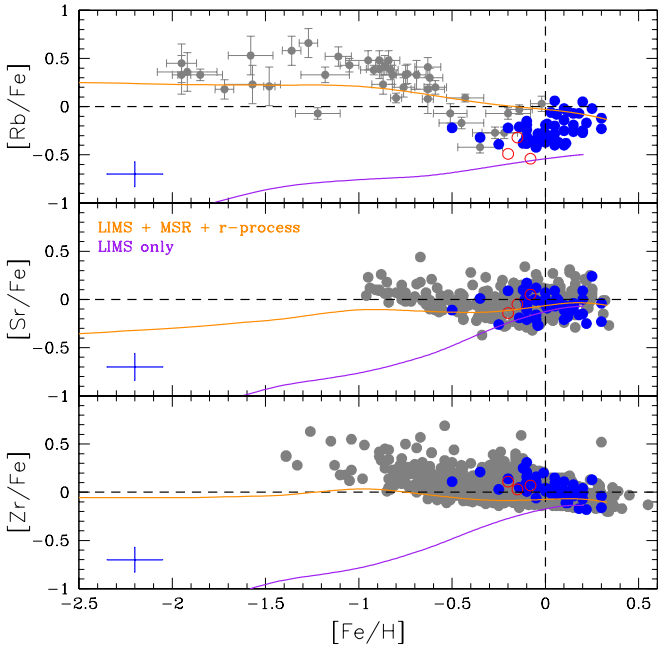

Fig. 5. [Rb,Sr,Zr/Fe] vs. [Fe/H] diagrams, *from top to bottom*. In the three panels, blue filled circles are our program stars. *Top panel*: grey dots with error bars are the [Rb/Fe] ratios derived in halo and disc giant and dwarf stars by Gratton & Sneden (1994) and Tomkin & Lambert (1999). *Middle and bottom panels*: grey dots are the [Sr/Fe] ratios derived by Mishenina et al. (2019), and [Zr/Fe] ratios by Battistini & Bensby (2016) and Delgado Mena et al. (2017), both in thin disc dwarf stars. A typical error bar in the [X/Fe] ratios for our M dwarfs is shown in the bottom left corner of each panel. For dwarf and giant stars (grey dots) the error bars are slightly smaller, which we have omitted for clarity. The red open circles in all the panels are the stars in which the Rb lines may be affected by magnetic field. Continuous lines are theoretical GCE predictions by Prantzos et al. (2018, 2020). Orange lines include the contributions from low- and intermediate-mass stars (LIMS), rotating massive stars (MSR), and the r-proces. Magenta lines include only LIMS.

The Rb underabundances found in our M dwarfs are unexpected and require further discussion. We cannot exclude systematic errors in the analysis, such as the existence of unknown blends in the Rb I lines, although there is no evidence of this. In particular, in our program stars, the strengthening of the line with decreasing $T_{\rm eff}$ is consistent with the behaviour of a resonance line of a heavy-element neutral species. The very well known blend at $\lambda \sim 7800$ Å with a Si I line is not expected to play any role here because of its high excitation energy ($\chi = 6.18$ eV) and the low $T_{\rm eff}$ of our stars. Another possibility is incorrect placement of the spectral continuum. We explored this possibility by changing its position up (down) by a given fraction. However, this led systematically to unrealistically large (small) Ti or/and O abundances from fits to the TiO lines in this region. On the other hand, underestimation of $T_{\rm eff}$ would lead systematically to the derived low Rb abundances, but differences of at least as large as ∼150 K would be required to explain this Rb underabundance. Although such a systematic error in $T_{\rm eff}$ cannot be fully excluded, this would also imply a significant change in the derived Sr and Zr abundances, which would be translated into a disagreement between the [Sr,Zr/Fe] ratios in M and FGK dwarfs (see Fig. 5). Systematic errors in the other stellar parameters at the level of the expected uncertainties have only a minor impact on the derived Rb abundance. In this respect, the most important parameter is C/O. However, we verified that unrealistically low

O and C abundances would be required to remove the observed Rb deficiency (which would also affect the fits of the TiO lines in the Rb spectral region).

We also explored possible correlations of the Rb abundance with the adopted $T_{\rm eff}$ and $\log g$. While there is no correlation with $T_{\rm eff}$, we found a weak correlation with $\log g$, namely larger Rb abundances for decreasing $\log g$ (correlation coefficient $r = 0.44$). This correlation, although weak, could be related with the stellar age. Evolutionary tracks show that M dwarfs of $Z \sim 0.014$ and $\log g \lesssim 4.6$ dex may have young ages because they are still contracting quasi-hydrostatically towards the main sequence (Bressan et al. 2012; Tang et al. 2014; Baraffe et al. 2015). Effects of low gravity in spectra of very young M (and L) dwarfs have been observed in stellar kinematic groups and the 125 Ma-old Pleiades open cluster (Mohanty & Basri 2003; Cruz et al. 2009; Shkolnik et al. 2009; Zapatero Osorio et al. 2014; Alonso-Floriano et al. 2015). Interestingly, the overwhelming majority of the stars in our sample with $\log g < 4.7$ dex have [Fe/H] > +0.15 dex and therefore may be relatively young. However, stellar chromospheric activity is observationally known to decline steeply with stellar age for solar-type field dwarfs that are younger than the Sun, and thereafter continues to decrease very slowly as stars get significantly older (Soderblom 2010; Ramírez et al. 2014). This seems to be also the case for M dwarfs (see e.g. Delfosse et al. 1998; Pizzolato et al. 2003; Astudillo-Defru et al. 2017) and, since the resonance Rb lines form in the upper layers of the atmosphere, the formation of these lines could be affected by the stellar activity and thus lead to incorrect estimation of the Rb abundance.

Related to the stellar ages above, another possible effect to take into account for very active stars with strong magnetic fields is the Zeeman broadening of the spectral lines with large Landé factors. The affected lines are shallower when compared to those of a non-active star, and this can affect the abundance determination by spectral synthesis if the magnetic field is not included. We identified three stars in our sample, namely J11201–104 (LP 733–099), J15218+209 (OT Ser), and J18174+483 (TYC 3529–1437–1), with strong activity levels based on their Hα emission from the CARMENES activity indicator analysis (Schöfer et al. 2019). By comparison with non-active stars of the same spectral type, we confirmed that in the three cases both Rb lines are indeed affected by Zeeman broadening (Fig. 6). For these three stars, the Rb abundances are amongst the lowest derived in the sample, and are consequentially highly uncertain (see Table A.1).We plot them with red open circles in Fig. 5. Nevertheless, even excluding these active stars and those with $\log g \lesssim 4.7$ dex from our analysis, the [Rb/Fe] deficiency and the positive correlation with [Fe/H] still remains (showing a slightly higher correlation, $r \sim 0.47$). On the other hand, no correlation is found between the derived Sr and Zr abundances with $T_{\rm eff}$ and $\log g$.

There could be other possibilities. Indeed, Lambert et al. (1995) found a similar problem when deriving Rb abundances in evolved cool M giants. These latter authors obtained systematic Ti underabundances from TiO lines in the region of the Rb lines, which is at odds with the metallicity derived from atomic lines. They discussed different possibilities to explain this effect, but could only solve this problem by adding an extra quasi-continuous opacity κ(TiO) in the spectral synthesis. They also showed that the Rb abundance expressed as [Rb/Fe] was almost insensitive to the chosen combination of quasi-continuous opacity and Ti abundances as long as [Fe/H] is derived from metallic lines around the Rb I lines (see Sect. 2). However, we did not find this issue here, as the metallicty

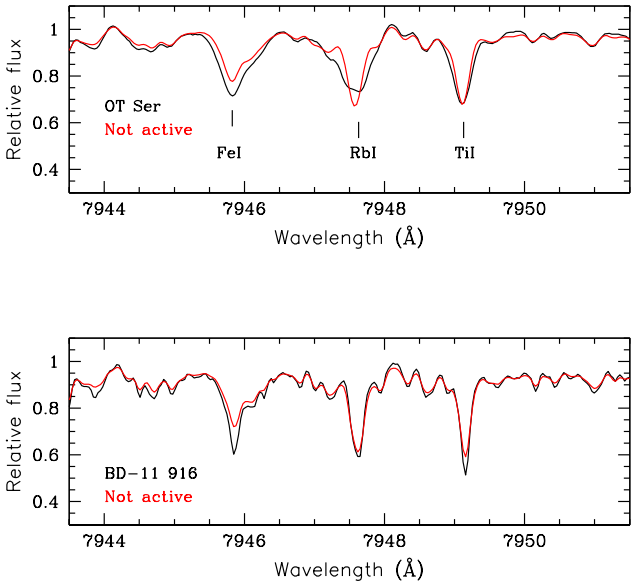

Fig. 6. Normalised spectra around the Rb I λ7947 Å line of stars with strong (J15218+209, OT Ser, M1.5 V, *top*, black line) and faint magnetic field (J04376–110, BD-11 916, M1.5 V, *bottom*, black line), in comparison with the spectra of a CARMENES GTO, slowly rotating inactive star of the same spectral type (J16254+543, GJ 625, M1.5 V, red line) broadened to the corresponding target star $v \sin i$.

inferred from the TiO lines around the Rb spectral region is compatible (within the uncertainty) with that derived from individual metallic lines in the other spectral ranges. Therefore, other possibilities have to be explored. For instance, it is well known that the Rb abundance in the Sun is rather controversial (Lodders 2019). Initial determinations by Withbroe (1971), Ross & Aller (1976), Anders & Grevesse (1989), and Palme & Jones (2003), among others, obtained 2.60 with very little dispersion. This value is significantly higher than the meteoritic value derived from CI chondrites (2.36 ± 0.03; e.g. Lodders & Palme 2009). Later, Grevesse et al. (2015) reduced this discrepancy and determined 2.47 ± 0.07 dex using a 3D atmosphere model for the Sun, but still ∼0.1 dex larger than the meteoritic value. While our non-LTE abundance (2.35 ± 0.02 dex; see Sect. 2) is in nice agreement with the meteoritic value, it seems that the issue may no longer be with the Rb in the Sun, but perhaps with the Sun in respect to the nearby stars.

There is some observational evidence that Rb in the Solar System could be overabundant with respect to the local ISM. Neutral Rb is expected to follow the spatial trend of neutral K (another alkali element) in interstellar clouds because these latter have similar ionisation potentials and chemical properties and therefore a determination of the interstellar elemental Rb/K ratio may provide insight into this issue. While the alkali ratios Li/K and Na/K measured in the local ISM (Welty & Hobbs 2001) are consistent with those in the Solar System, this is not the case for Rb/K. Walker et al. (2009) studied Rb/K toward seven different ISM directions from the Sun and obtained values ∼34% lower than the meteoritic (solar) value, except perhaps towards ρ Oph A. The condensation temperature for Rb is lower than that for K. As a result, if depletion onto grains was the only deciding factor then one would expect a higher Rb/K, contrary to the observational results. Depletion patterns in the local ISM are not always found for elements with similar condensation temperatures to that of Rb. For example, Cartledge et al. (2006) found a depletion by ∼25% in Ge with respect to the meteoritic value

but no evidence for Cd and Sn. This result led Walker et al. (2009) to suggest that neutron capture elements synthesised by the weak s-process and the r-process in massive stars (as Rb) appear to show significantly lower interstellar abundances than seen in the Solar System when compared with those synthesised mainly in low-mass stars. However, Ritchey et al. (2018), in a more comprehensive study on the depletion pattern of several neutron-capture elements (Ge, Ga, As, Kr, Cd, etc.) in the local ISM, concluded that a simple dichotomy between the production of heavy elements by low- and high-mass stars cannot account for the unexpectedly low interstellar abundance of Rb and other neutron capture elements. The value found here for M dwarfs, if confirmed, may open this discussion again. To elucidate this, K abundance determinations are suggested in M dwarfs. Unfortunately, most K I lines identified in the CARMENES spectra of M dwarfs are very strong and are affected by magnetic activity (Fuhrmeister et al., in prep.). Accepting the [Rb/Fe] discussed above as genuine, in the following section we compare our observational results with a Galactic chemical evolution (GCE) model for neutron-capture elements in order to extract information about possible nucleosynthetic implications.

3.1. Comparison with GCE models

Figure 5 compares the observed [Rb,Sr,Zr/Fe]-versus-[Fe/H] trends with the theoretical predictions according to the GCE model from Prantzos et al. (2018, 2020) for the solar neighbourhood. This model is a state-of-the-art one-zone GCE model as far as the neutron capture elements are concerned, which uses recent yields from LIMS (Cristallo et al. 2015), as well as of massive rotating stars (MSRs; Limongi & Chieffi 2018). The former are the main contributors to neutron-capture elements formed through the main component of the s-process, while the latter contribute through the weak s-process, for which the inclusion of stellar rotation becomes critical. The r-process is assumed in this GCE model to be associated to the evolution of massive stars. For Rb, at the time of the Solar System formation, this GCE model predicts s- and r-fractions of 51 and 49% (33, 67% for ^{85}Rb; 96, 4% for ^{87}Rb), and 91.2, 73, 82% (s-fraction) and 8.3, 22, 18% (r-fraction) for the light heavy elements Sr, Y, and Zr, respectively[8]. We note that the model accounts for the observed Solar System abundances of most of the heavy elements ($Z > 30$) within 10%. A detailed description of this GCE model, as well as of the stellar yields used, can be found in Prantzos et al. (2018, 2020).

We compare the model predictions with observations in two illustrative cases in Fig. 5: the orange line shows the predicted relationships when all the nucleosynthetic sources are included (LIMS, MSR, and r-process), which we refer to as the "baseline" model, while the magenta line shows the result when only the LIMS contribution is considered (i.e. the main s-process contribution). The baseline model considerably better reproduces the average observed [Rb/Fe]-versus-[Fe/H] trend at low metallicity ([Fe/H] $\lesssim -1.0$; top panel of Fig. 5), where the [Rb/Fe] ratio is almost flat ($\sim +0.3$ dex; i.e. it has a primary behaviour), similar to that observed for a genuine r-process element (e.g. Eu; Mashonkina et al. 2003; Zhao et al. 2016; Delgado Mena et al. 2017). We conclude that at low metallicity the r-process is the main source of Rb, although with a non-negligible contribution from the weak s-process occurring in MRS. The Rb production from LIMS has a secondary behaviour (magenta line) and only becomes significant at [Fe/H] $\gtrsim -0.3$ (see Fig. 5, top panel). At [Fe/H] $\gtrsim -1.0$, the observed [Rb/Fe] ratio declines in a similar way as other primary elements (or elements with a main r-process origin) due to the increasing contribution to Fe from type Ia supernovae. However, contrary to what is typically observed for these elements, the [Rb/Fe] ratio reaches ~0.0 at a lower metallicity and is below the solar ratio at [Fe/H] ≈ 0.0 according to our observational results. We note that Gratton & Sneden (1994) and Tomkin & Lambert (1999) also derived [Rb/Fe] < 0.0 in a few stars with [Fe/H] > -1.0[9]. This is an unexpected result and has not been observed in any other heavy element. Typically most of the heavy elements show average solar ratios ([X/Fe]) at [Fe/H] $\sim$ 0, but not systematically below solar, as can be seen, for instance, in the [Sr,Zr/Fe]-versus-[Fe/H] relationships (middle and lower panels of Fig. 5). The observed behaviour of the [Sr,Zr/Fe] ratios is reasonably well reproduced by our baseline model. However, this baseline model cannot reproduce the observed [Rb/Fe] ratios at [Fe/H] $\gtrsim -1.0$. This fact would imply at least two things: (*a*) the Rb production in massive stars is overestimated in the GCE model at these metallicities; and (*b*) because of the time delay of the AGB stars producing cosmic Rb, their contribution is theoretically predicted to start contributing at metallicities higher than [Fe H] ~ -0.7 (Bisterzo et al. 2014; Prantzos et al. 2018). However, as seen in Fig. 5, the contribution from AGB stars is not enough to explain the observed [Rb/Fe] ratios at nearly solar metallicity. We note that Rb yields from different AGB stellar models (e.g. Karakas & Lattanzio 2014) may be systematically larger with respect to those by Cristallo et al. (2015) adopted in Prantzos et al. (2018). These differences are due to different prescriptions used for mixing and mass-loss rates. However, in this case the yields of other heavy elements produced by the s-process, such as Sr, Y and Zr in particular, are also enhanced, resulting in a probable overproduction of these elements, which is not required according to our GCE model (see Fig. 5, middle and bottom panels).

As mentioned before, for metallicities above solar, we found an increasing [Rb/Fe] trend, which would imply a secondary behaviour with metallicity. This trend is surprising, because according to GCE models, the Fe contribution from type Ia supernovae should nominally decrease the trend. The secondary nature of this trend excludes a standard r-process contribution, while it could favour a s-process scenario. The Rb s-process production is indeed secondary in both non-rotating massive stars and AGB stars. This production is related to the activation of the ^{22}Ne$(\alpha, n)^{25}$Mg neutron source, whose efficiency increases with metallicity because of the larger amount of ^{22}Ne left by the burning of CNO[10]. In AGB stars in particular, this neutron source is active during the thermal pulses when the temperature in the He-shell attains or exceeds ~300 MK. However, in low-mass AGB stars, which are the galactic polluters responsible for the production of the s-process main component, the ^{22}Ne$(\alpha, n)^{25}$Mg is only marginally activated because of the low temperature developed during the thermal pulses. In contrast, the main neutron source, namely ^{13}C$(\alpha, n)^{16}$O, is active during the interpulse phase, when the temperature is ~90 MK, but the resulting neutron density is much lower than the threshold needed to open the ^{85}Kr (ground

[8] There is a 0.5% fraction contribution for Sr due to the p-process.

[9] We have scaled the [Rb/Fe] ratios derived by these authors to the solar Rb abundance (2.47) adopted here.

[10] At the end of the H burning, the initial amount of C+N+O is mostly transformed into ^{14}N. Later on, when the He burning starts, ^{22}Ne is produced by the chain ^{14}N$(\alpha, \gamma)^{18}$F$(\beta)^{18}$O$(\alpha, \gamma)^{22}$Ne. In practice, the initial amount of C+N+O is transformed into ^{22}Ne. This scenario is altered if rotation-induced mixing brings fresh C, as synthesised by the He burning, into the H-burning shell.

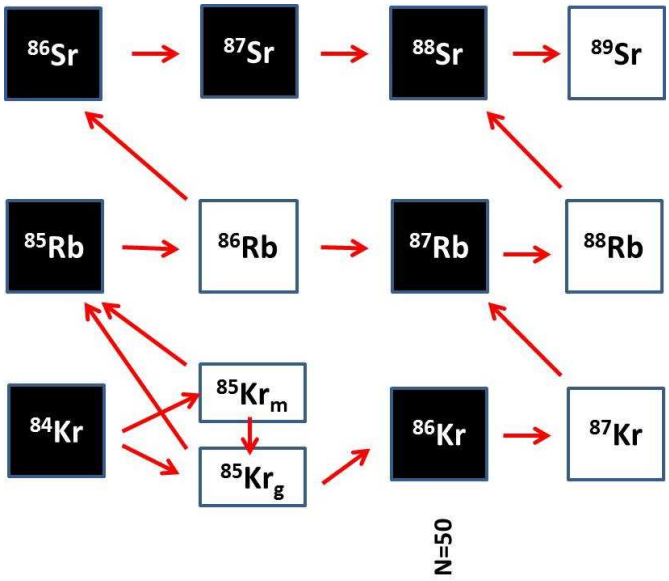

Fig. 7. Scheme illustrating the operation of the two branches at ^{85}Kr (ground state) and ^{86}Rb that determine the Rb production by the s-process. Black filled nuclei are stable, while the empty ones are unstable. Arrows show possible nuclear reactions, particularly neutron captures or β-decays. In case of low neutron density ($N_n < 10^9$ cm^{-3}), both branches are closed and the s-process follows the chain ^{84}Kr $\rightarrow^{85}$ Kr $\rightarrow^{85}$ Rb $\rightarrow^{86}$ Rb $\rightarrow^{86}$ Sr. Owing to the large neutron-capture cross section of ^{85}Kr compared to those of the neutron-magic nuclei ($N = 50$) ^{88}Sr, ^{89}Y, and ^{90}Zr, a low amount of Rb is produced. On the contrary, at higher neutron density, the two branches are open and the s-process sequence deviates toward ^{86}Kr and ^{87}Rb, both of which are neutron magic nuclei, and therefore both present very low neutron-capture cross sections. In the latter case, large overabundances of Kr and Rb are found.

state) and ^{86}Rb branches. This occurrence is illustrated in Fig. 7. As a result, low [Rb/Sr, Y, Zr] ratios are expected.

An interesting deviation from the standard AGB scenario illustrated so-far was firstly described by Cristallo et al. (2009; see also Karakas 2010; Cristallo et al. 2018). At nearly solar metallicity, the ^{13}C is not completely burnt during the interpulse and part of it is engulfed in the convective shell generated by the following thermal pulse and burned at higher temperature (~200 MK). The resulting neutron density is high enough to open the ^{85}Kr and ^{86}Rb branches, allowing the production of the neutron magic rubidium isotope: ^{87}Rb. In this case, owing to the low neutron-capture cross section of this magic nucleus, an overproduction of Rb is expected, while Sr, Y, and Zr, which are mainly produced by the interpulse ^{13}C burning, are not affected. The occurrence of this additional ^{13}C neutron burst requires particularly low interpulse temperatures, and in turn low core masses. For this reason, it may only occur in AGB stars with low masses ($M \lesssim 3\ M_\odot$) and high metallicities ([Fe/H] > -0.1). An important ingredient of the theoretical stellar models that hampers a definite validation of this hypothesis is our poor knowledge of the ^{13}C$(\alpha, n)^{16}$O reaction (Cristallo et al. 2018). In this context, a lower rate at $T \sim 90$ MK would greatly enhance the contribution to the galactic Rb of low-mass AGB stars at nearly solar and super-solar metallicity. It is possible that the observed high-metallicity trend of galactic Rb shown in Fig. 5 (top panel) is a hint in favour of this scenario.

A similar trend of increasing [Ba/Fe] with increasing metallicity was reported at young ages in solar twins, open clusters, and local associations (e.g. D'Orazi et al. 2012; Reddy & Lambert 2015; Nissen 2016; Tabernero et al. 2017). However, this trend is not seen for other heavy elements of similar s-process origin (e.g. La, Nd). To account for this Ba trend, Maiorca et al. (2012) suggested that the observed enhancement can be produced by nucleosynthesis in AGB stars of low mass ($M < 1.5\ M_\odot$) if they release neutrons from the ^{13}C$(\alpha$,n$)^{16}$O reaction in reservoirs larger by a factor of four than assumed in more massive AGB stars ($M > 1.5\ M_\odot$). Mishenina et al. (2015) instead reintroduced the intermediate neutron-capture i-process discussed earlier by Cowan & Rose (1977) to explain this fact, in which the neutron density operating the process is approximately 10^{15} cm^{-3}. Also, recently Ryde et al. (2020) found a secondary behaviour of [F/Fe] for supersolar metallicities in K giants. We note that F has a significant cosmic contribution from AGB stars (Jorissen et al. 1992; Karakas & Lattanzio 2014; Abia et al. 2019). Although F is produced in AGB stars from an alternative nuclear channel to the s-elements, its production needs neutrons and is therefore linked to the s-process (see e.g. Cristallo et al. 2014; Abia et al. 2019). Nevertheless, as far as the [Ba/Fe] ratio is concerned this trend has recently been shown to be correlated with the stellar activity of young stars and to not be nucleosynthetic in origin (Reddy & Lambert 2017). Some of the stars studied here were flagged as active by Passegger et al. (2019), but except for the three stars mentioned above, we checked that the rest of the stars flagged as active are distributed uniformly within the range of [Rb/Fe] ratios derived here. In any case, a detailed study of possible connection between stellar activity and Rb abundances is suggested in M dwarfs without showing any peculiar abundance pattern.

Another valuable piece of information on the production sources of Rb and its evolution with metallicity comes from its abundance ratio with respect to the neighbouring s-elements Sr, Y, and Zr. As mentioned in Sect. 1 this abundance ratio provides relevant information on the physical conditions prevailing at the s-process site, in particular about the neutron density. This may allow, for instance, the characteristic stellar mass of the producing objects to be inferred. Figure 8 shows the [Rb/⟨Sr+Zr⟩]-versus-[Fe/H] ratios derived in our stars (blue dots), as well as in the studies by Gratton & Sneden (1994), Tomkin & Lambert (1999), and Mishenina et al. (2019) in FGK dwarfs (grey dots). ⟨Sr+Zr⟩ is the average ratio between [Sr/H] and [Zr/H] in the corresponding star. As in Fig. 5, the orange line is the theoretical prediction according to the GCE model by Prantzos et al. (2018), which includes LIMS, MRS, and the r-process contributions, while the magenta line is the prediction when only yields from LIMS are included. Figure 8 also shows the prediction in the case where rotation is excluded in massive stars (black line), that is, the weak s-process contribution is strongly inhibited. At low metallicity ([Fe/H] < -1.0) the observed [Rb/⟨Sr+Zr⟩] ratio is above the solar value and again is better reproduced when all the possible production sources of Rb are included (orange line). We note that the observed trend does not change significantly if non-LTE Rb abundances are used. At these metallicities, the r-process dominates the production of Rb, Sr, and Zr but, as mentioned before, there is a non-negligible contribution from the weak s-process in massive stars as can be appreciated by comparison with the prediction with no weak s-process (black line). At the typical neutron densities of the weak s-process ($N_n \sim 10^{11-13}$ cm^{-3}), some branchings, closed in the case of the ^{13}C$(\alpha$,n$)^{16}$O neutron source, are opened (see Fig. 7). This allows alternative paths, in particular that at the ^{85}Kr, which leads to an overproduction of Rb with respect to Sr and Zr, giving [Rb/⟨Sr+Zr⟩] ≥ 0.0. We note that the ^{22}Ne$(\alpha$,n$)^{25}$Mg source becomes relevant even for stellar masses as low as ~2.5 $M_\odot$ and

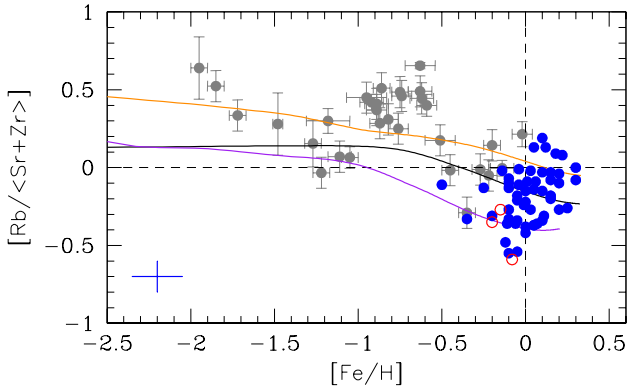

Fig. 8. Same as Fig. 5 but for [Rb/⟨Sr+Zr⟩] vs. [Fe/H]. Blue dots are M dwarfs in this study. Grey dots corresponds to the giants and dwarfs stars analysed in common by Gratton & Sneden (1994), Tomkin & Lambert (1999), and Mishenina et al. (2019). Red open circles are stars in which Rb lines may be affected by the magnetic field. Coloured solid lines are the GCE predictions as in Fig. 5. The black solid line shows the GCE prediction when the weak s-process is inhibited in massive stars (i.e. no rotation).

$Z \lesssim 0.01\,Z_{\odot}$ (Straniero et al. 2014). Figure 8 shows that as metallicity increases, the [Rb/⟨Sr+Zr⟩] diminishes and is below solar on average for [Fe/H] ∼ 0.0, although with a significant dispersion. This dispersion is considerably larger than expected from the uncertainties in the analysis and may therefore be real. The decrease in the [Rb/⟨Sr+Zr⟩] ratio for increasing metallicity is clearly due to the increasing relevance of the contribution of low-mass stars in the production of Rb, Sr, and Zr through the main s-process, for which the $^{13}C(\alpha,n)^{16}O$ is the main neutron source. When this neutron source is at work, [Rb/⟨Sr+Zr⟩] < 0.0 is expected, as shown by GCE model (magenta line). Nevertheless, in Fig. 8 there are a number of stars showing [Rb/⟨Sr+Zr⟩] $\gtrsim$ 0.0. If the Rb abundances in these stars were correct (see the discussion above), these ratios would be better explained if massive (intermediate) AGB stars contribute significantly at [Fe/H] $\gtrsim$ 0.0. In summary, with the available yields for Rb from different sources, the observed [Rb/⟨Sr+Zr⟩] ratios at near-solar metallicity seem to require a mix of these contributing sources. It is obvious that determinations of Rb abundances in FGK dwarf stars, the analysis of which is subject to less uncertainties, are needed to shed light on this Rb puzzle.

4. Summary

We derived, for the first time, abundances of Rb and its associated elements Sr and Zr in a sample of M dwarfs in the close solar neighbourhood and in the metallicity range −0.5 $\lesssim$ [Fe/H] $\lesssim$ +0.3. These metallicity and spectral type ranges were poorly explored in previous studies for Rb abundances. We used high-resolution and high-S/N spectra in the VIS and NIR acquired with the CARMENES spectrograph. The main novel result of our study is that, in the explored metalliciy range and relative to the metallicity, rubidium is systematically underabundant with respect to the Sun. This underabundance is of almost a factor two on average, although with significant dispersion. This result is in contrast with the figure found for Sr and Zr ratios with respect to the metallicity, which are very close to the solar ratio, and is identical to that found in unevolved FGK dwarfs of similar metallicity. Furthermore, we find a possible positive correlation of the [Rb/Fe] ratio with increasing metallicity. We discuss the reliability of these results for Rb, never found for other neutron-capture element in the metallicity range studied here, in terms of non-LTE effects, systematic errors in the analysis, anomalous Solar System Rb abundance, and stellar activity, but no plausible explanation is found.

Under the assumption that the abundance trend is real, we interpret the [Rb/Fe]-versus-[Fe/H] relationship in the observed full range of metallicity by comparing it with theoretical predictions from state-of-the-art one-dimensional GCE models for neutron-capture elements in the solar neighbourhood (Prantzos et al. 2018). The observed Rb overabundances at [Fe/H] $\lesssim -1.0$ can be explained if the r-process is the main source of the Galactic Rb budget at these metallicities, although with a significant contribution from the weak s-process occurring in rotating massive stars. However, the [Rb/Fe] underabundances observed at higher metallicities cannot be reproduced by this model, nor can the possible secondary behaviour of [Rb/Fe] with metallicity. This secondary behaviour would require a much higher Rb yield from AGB stars through the main s-process than is currently obtained in s-process nucleosynthesis calculations without overproducing Sr, Y, and Zr. A possible nucleosynthesis scenario occurring in low-mass and high-metallicity AGB stars is suggested. In addition, the negative [Rb/⟨Sr+Zr⟩] ratios observed at near solar and higher metallicities, when compared with the GCE predictions, indicate that AGB stars are indeed the main producers of Rb at these metallicities, although the large scatter observed suggests that there are other contributing sources.

Overall, our abundance analysis showcases the value of abundance determinations in M dwarfs for Galactic chemical evolution studies. Additional Rb abundance measurements in FGK dwarfs of near solar metallicity, as well as an evaluation of the impact of stellar activity on abundance determinations in M dwarfs, are urgently needed to confirm or disprove the main findings of this study.

Acknowledgements. CARMENES is an instrument for the Centro Astronómico Hispano-Alemán (CAHA) at Calar Alto (Almería, Spain), operated jointly by the Junta de Andalucía and the Instituto de Astrofísica de Andalucía (CSIC). CARMENES was funded by the Max-Planck-Gesellschaft (MPG), the Consejo Superior de Investigaciones Científicas (CSIC), the Ministerio de Economía y Competitividad (MINECO) and the European Regional Development Fund (ERDF) through projects FICTS-2011-02, ICTS-2017-07-CAHA-4, and CAHA16-CE-3978, and the members of the CARMENES Consortium (Max-Planck-Institut für Astronomie, Instituto de Astrofísica de Andalucía, Landessternwarte Königstuhl, Institut de Ciències de l'Espai, Institut für Astrophysik Göttingen, Universidad Complutense de Madrid, Thüringer Landessternwarte Tautenburg, Instituto de Astrofísica de Canarias, Hamburger Sternwarte, Centro de Astrobiología and Centro Astronómico Hispano-Alemán), with additional contributions by the MINECO, the Deutsche Forschungsgemeinschaft through the Major Research Instrumentation Programme and Research Unit FOR2544 "Blue Planets around Red Stars", the Klaus Tschira Stiftung, the states of Baden-Württemberg and Niedersachsen, and by the Junta de Andalucía. We acknowledge financial support from the Agencia Estatal de Investigación of the Ministerio de Ciencia e Innovación, the Universidad Complutense de Madrid, the Fundação para a Ciência e a Tecnologia, the Generalitat de Catalunya, ERDF, and NASA through projects PGC2018-095317-B-C21, PID2019-109522GB-C51/2/3/4, PGC2018-098153-B-C33, AYA2016-79425-C3-[1,2,3]-P, FPU15/01476, UID[B,P]/04434/2020, PTDC/FIS-AST/28953/2017, POCI-01-0145-FEDER-028953, SEV-2015-0548, SEV-2017-0709, MDM-2017-0737, NNX17AG24G, and the CERCA programme. Finally, we thank Verne Smith, Katia Cunha, and the APOGEE/ASPCAP team for the APOGEE line list, and K. Lodders for her useful comments on the manuscript.

References

Abia, C., & Wallerstein, G. 1998, MNRAS, 293, 89
Abia, C., Busso, M., Gallino, R., et al. 2001, ApJ, 559, 1117
Abia, C., Cristallo, S., Cunha, K., de Laverny, P., & Smith, V. V. 2019, A&A, 625, A40

Allen, C. W. 1973, Astrophysical quantities (London: University of London, Athlone Press)
Alonso-Floriano, F. J., Morales, J. C., Caballero, J. A., et al. 2015, A&A, 577, A128
Anders, E., & Grevesse, N. 1989, Geochim. Cosmochim. Acta, 53, 197
Andrievsky, S. M., Spite, F., Korotin, S. A., et al. 2011, A&A, 530, A105
Arnett, W. D., & Thielemann, F. K. 1985, ApJ, 295, 589
Arnould, M., & Goriely, S. 2020, Prog. Part. Nucl. Phys., 112, 103766
Astudillo-Defru, N., Delfosse, X., Bonfils, X., et al. 2017, A&A, 600, A13
Baraffe, I., Homeier, D., Allard, F., & Chabrier, G. 2015, A&A, 577, A42
Barklem, P. S., Piskunov, N., & O'Mara, B. J. 2000, A&AS, 142, 467
Battistini, C., & Bensby, T. 2016, A&A, 586, A49
Belyakova, E. V., & Mashonkina, L. I. 1997, AZh, 74, 601
Bergemann, M., Hansen, C. J., Bautista, M., & Ruchti, G. 2012, A&A, 546, A90
Birky, J., Hogg, D. W., Mann, A. W., & Burgasser, A. 2020, ApJ, 892, 31
Bisterzo, S., Travaglio, C., Gallino, R., Wiescher, M., & Käppeler, F. 2014, ApJ, 787, 10
Bisterzo, S., Travaglio, C., Wiescher, M., Käppeler, F., & Gallino, R. 2017, ApJ, 835, 97
Bressan, A., Marigo, P., Girardi, L., et al. 2012, MNRAS, 427, 127
Brewer, M.-M., & Carney, B. W. 2006, AJ, 131, 431
Bruls, J. H. M. J., Rutten, R. J., & Shchukina, N. G. 1992, A&A, 265, 237
Busso, M., Gallino, R., & Wasserburg, G. J. 1999, ARA&A, 37, 239
Caballero, J. A., Cortés-Contreras, M., Alonso-Floriano, F. J., et al. 2016a, in 19th Cambridge Workshop on Cool Stars, Stellar Systems, and the Sun (CS19), 148
Caballero, J. A., Guàrdia, J., López del Fresno, M., et al. 2016b, SPIE Conf. Ser., 9910, 99100E
Carlsson, M. 1986, Uppsala Astronomical Observatory Reports, 33
Cartledge, S. I. B., Lauroesch, J. T., Meyer, D. M., & Sofia, U. J. 2006, ApJ, 641, 327
Cortes-Contreras, M. 2016, PhD thesis, Universidad Complutense de Madrid, Spain
Cowan, J. J., & Rose, W. K. 1977, ApJ, 217, 51
Cowan, J. J., Sneden, C., Lawler, J. E., et al. 2019, Rev. Mod. Phys., submitted [arXiv:1901.01410]
Cristallo, S., Straniero, O., Gallino, R., et al. 2009, ApJ, 696, 797
Cristallo, S., Piersanti, L., Straniero, O., et al. 2011, ApJS, 197, 17
Cristallo, S., Di Leva, A., Imbriani, G., et al. 2014, A&A, 570, A46
Cristallo, S., Straniero, O., Piersanti, L., & Gobrecht, D. 2015, ApJS, 219, 40
Cristallo, S., La Cognata, M., Massimi, C., et al. 2018, ApJ, 859, 105
Cruz, K. L., Kirkpatrick, J. D., & Burgasser, A. J. 2009, AJ, 137, 3345
Cunha, K., Smith, V. V., Hasselquist, S., et al. 2017, ApJ, 844, 145
de Laverny, P., Abia, C., Domínguez, I., et al. 2006, A&A, 446, 1107
Delfosse, X., Forveille, T., Perrier, C., & Mayor, M. 1998, A&A, 331, 581
Delgado Mena, E., Tsantaki, M., Adibekyan, V. Z., et al. 2017, A&A, 606, A94
D'Orazi, V., Biazzo, K., Desidera, S., et al. 2012, MNRAS, 423, 2789
Drawin, H.-W. 1968, Z. Phys., 211, 404
Gaidos, E., Mann, A. W., Lépine, S., et al. 2014, MNRAS, 443, 2561
Gallino, R., Arlandini, C., Busso, M., et al. 1998, ApJ, 497, 388
García-Hernández, D. A., García-Lario, P., Plez, B., et al. 2006, Science, 314, 1751
García-Hernández, D. A., Manchado, A., Lambert, D. L., et al. 2009, ApJ, 705, L31
Gratton, R. G., & Sneden, C. 1994, A&A, 287, 927
Grevesse, N., Scott, P., Asplund, M., & Sauval, A. J. 2015, A&A, 573, A27
Gustafsson, B., Edvardsson, B., Eriksson, K., et al. 2008, A&A, 486, 951
Hasselquist, S., Shetrone, M., Cunha, K., et al. 2016, ApJ, 833, 81
Heiter, U., Lind, K., Asplund, M., et al. 2015, Phys. Scr., 90, 054010
Hinkle, K., Wallace, L., & Livingston, W. 1995, PASP, 107, 1042
Husser, T. O., Wende-von Berg, S., Dreizler, S., et al. 2013, A&A, 553, A6
Jofré, P., Heiter, U., & Soubiran, C. 2019, ARA&A, 57, 571
Jorissen, A., Smith, V. V., & Lambert, D. L. 1992, A&A, 261, 164
Käppeler, F., Gallino, R., Bisterzo, S., & Aoki, W. 2011, Rev. Mod. Phys., 83, 157
Karakas, A. I. 2010, Astrophys. Space Sci. Proc., 16, 107
Karakas, A. I., & Lattanzio, J. C. 2014, PASA, 31, e030
Kirkpatrick, J. D., Henry, T. J., & McCarthy, Donald W., J. 1991, ApJS, 77, 417
Korotin, S. A. 2020, Astron. Lett., 46, 541
Korotin, S. A., Andrievsky, S. M., & Luck, R. E. 1999, A&A, 351, 168
Lambert, D. L., Smith, V. V., Busso, M., Gallino, R., & Straniero, O. 1995, ApJ, 450, 302
Limongi, M., & Chieffi, A. 2018, ApJS, 237, 13
Lodders, K. 2019, The Oxford Research Encyclopedia of Planetary Science (Oxford: Oxford University Press
Lodders, K., & Palme, H. 2009, Meteorit. Planet. Sci. Suppl., 72, 5154
Maiorca, E., Magrini, L., Busso, M., et al. 2012, ApJ, 747, 53
Majewski, S. R., Schiavon, R. P., Frinchaboy, P. M., et al. 2017, AJ, 154, 94
Mann, A. W., Feiden, G. A., Gaidos, E., Boyajian, T., & von Braun, K. 2015, ApJ, 804, 64
Mashonkina, L., Gehren, T., Travaglio, C., & Borkova, T. 2003, A&A, 397, 275
Mishenina, T., Pignatari, M., Carraro, G., et al. 2015, MNRAS, 446, 3651
Mishenina, T., Pignatari, M., Gorbaneva, T., et al. 2019, MNRAS, 484, 3846
Mohanty, S., & Basri, G. 2003, ApJ, 583, 451
Morton, D. C. 2000, ApJS, 130, 403
Nagel, E., Czesla, S., Kaminski, A., et al. 2020, A&A, submitted
Nissen, P. E. 2016, A&A, 593, A65
Palme, H., & Jones, A. 2003, Treatise Geochem., 1, 711
Park, C. 1971, J. Quant. Spectr. Rad. Transf., 11, 7
Passegger, V. M., Reiners, A., Jeffers, S. V., et al. 2018, A&A, 615, A6
Passegger, V. M., Schweitzer, A., Shulyak, D., et al. 2019, A&A, 627, A161
Pérez-Mesa, V., Zamora, O., García-Hernández, D. A., et al. 2017, A&A, 606, A20
Peterson, R. C., Dalle Ore, C. M., & Kurucz, R. L. 1993, ApJ, 404, 333
Pian, E., D'Avanzo, P., Benetti, S., et al. 2017, Nature, 551, 67
Pignatari, M., Gallino, R., Heil, M., et al. 2010, ApJ, 710, 1557
Pizzolato, N., Maggio, A., Micela, G., Sciortino, S., & Ventura, P. 2003, A&A, 397, 147
Plez, B. 2012, Astrophysics Source Code Library [record ascl:1205.004]
Prantzos, N., Hashimoto, M., & Nomoto, K. 1990, A&A, 234, 211
Prantzos, N., Abia, C., Limongi, M., Chieffi, A., & Cristallo, S. 2018, MNRAS, 476, 3432
Prantzos, N., Abia, C., Cristallo, S., Limongi, M., & Chieffi, A. 2020, MNRAS, 491, 1832
Quirrenbach, A., Amado, P. J., Caballero, J. A., et al. 2014, SPIE Conf. Ser., 9147, 91471F
Quirrenbach, A., Amado, P. J., Ribas, I., et al. 2018, SPIE Conf. Ser., 10702, 107020W
Raiteri, C. M., Busso, M., Gallino, R., & Picchio, G. 1991, ApJ, 371, 665
Ramírez, I., Meléndez, J., Bean, J., et al. 2014, A&A, 572, A48
Reddy, A. B. S., & Lambert, D. L. 2015, MNRAS, 454, 1976
Reddy, A. B. S., & Lambert, D. L. 2017, ApJ, 845, 151
Reddy, B. E., Lambert, D. L., & Allende Prieto, C. 2006, MNRAS, 367, 1329
Reiners, A., Mrotzek, N., Lemke, U., Hinrichs, J., & Reinsch, K. 2016, A&A, 587, A65
Reiners, A., Zechmeister, M., Caballero, J. A., et al. 2018, A&A, 612, A49
Ritchey, A. M., Federman, S. R., & Lambert, D. L. 2018, ApJS, 236, 36
Ross, J. E., & Aller, L. H. 1976, Science, 191, 1223
Ryde, N., Edvardsson, B., Gustafsson, B., et al. 2009, A&A, 496, 701
Ryde, N., Jönsson, H., Mace, G., et al. 2020, ApJ, 893, 37
Schöfer, P., Jeffers, S. V., Reiners, A., et al. 2019, A&A, 623, A44
Schweitzer, A., Passegger, V. M., Cifuentes, C., et al. 2019, A&A, 625, A68
Seaton, M. J. 1962, Atomic and Molecular Processes, ed. D. R. Bates (New York: Academic Press)
Shkolnik, E., Liu, M. C., & Reid, I. N. 2009, ApJ, 699, 649
Sneden, C., Cowan, J. J., & Gallino, R. 2008, ARA&A, 46, 241
Soderblom, D. R. 2010, ARA&A, 48, 581
Souto, D., Cunha, K., Smith, V. V., et al. 2020, ApJ, 890, 133
Steenbock, W., & Holweger, H. 1984, A&A, 130, 319
Straniero, O., Cristallo, S., & Piersanti, L. 2014, ApJ, 785, 77
Tabernero, H. M., Montes, D., González Hernández, J. I., & Ammler-von Eiff, M. 2017, A&A, 597, A33
Tang, J., Bressan, A., Rosenfield, P., et al. 2014, MNRAS, 445, 4287
Thielemann, F. K., Eichler, M., Panov, I. V., & Wehmeyer, B. 2017, Ann. Rev. Nucl. Part. Sci., 67, 253
Tomkin, J., & Lambert, D. L. 1999, ApJ, 523, 234
Trifonov, T., Kürster, M., Zechmeister, M., et al. 2018, A&A, 609, A117
Tsuji, T., & Nakajima, T. 2014, PASJ, 66, 98
Vainshtein, L. A., Sobelman, I. I., & Iukov, E. A. 1979, Moscow Izdatel Nauka, 319
van Raai, M. A., Lugaro, M., Karakas, A. I., García-Hernández, D. A., & Yong, D. 2012, A&A, 540, A44
van Regemorter, H. 1962, ApJ, 136, 906
Veyette, M. J., Muirhead, P. S., Mann, A. W., et al. 2017, ApJ, 851, 26
Walker, K. M., Federman, S. R., Knauth, D. C., & Lambert, D. L. 2009, ApJ, 706, 614
Warner, B. 1968, MNRAS, 139, 115
Welty, D. E., & Hobbs, L. M. 2001, ApJS, 133, 345
Withbroe, G. L. 1971, in Solar Physics, Atomic Spectra, and Gaseous Nebulae, ed. K. B. Gebbie (London: Forgotten Books), 127
Yakovleva, S. A., Barklem, P. S., & Belyaev, A. K. 2018, MNRAS, 473, 3810
Yong, D., Aoki, W., Lambert, D. L., & Paulson, D. B. 2006, ApJ, 639, 918
Zapatero Osorio, M. R., Béjar, V. J. S., Martín, E. L., et al. 2014, A&A, 572, A67
Zechmeister, M., Reiners, A., Amado, P. J., et al. 2018, A&A, 609, A12
Zechmeister, M., Dreizler, S., Ribas, I., et al. 2019, A&A, 627, A49
Zhao, G., Mashonkina, L., Yan, H. L., et al. 2016, ApJ, 833, 225

Appendix A: Additional table

Table A.1. Stellar parameters and abundances derived in the sample of M dwarfs.

Karmn	Name	$T_{\rm eff}$ (K)	log g	C/O	[M/H]	log ϵ(Rb)	log ϵ(Sr)	log ϵ(Zr)
J00051+457	GJ 2	3772	4.68	0.59	0.10	2.32 ± 0.02	2.91	2.70
J00183+440	GX And	3606	4.77	0.61	−0.14	2.12 ± 0.05	2.58	2.50
J00389+306	G 60–10	3491	4.78	0.59	−0.10	2.22 ± 0.01	2.73	2.55
J00570+450	G 172–30	3397	4.85	0.50	−0.10	2.13 ± 0.01	2.90	2.80
J01013+613	GJ 47	3496	4.80	...	−0.11	2.00 ± 0.02	2.80	2.55 ± 0.02
J01025+716	GJ 48	3432	4.78	0.47	0.00	2.19 ± 0.01	2.85	2.60
J01026+623	BD+61 195	3810	4.67	0.54	0.06	2.45	2.98	2.63
J01433+043	G 3–14	3485	4.80	0.50	−0.10	1.99 ± 0.03	2.70	2.60 ± 0.01
J01518+644	G 244–37	3666	4.64	0.58	0.20	2.42 ± 0.02	2.96	2.72 ± 0.02
J02015+637	G 244–47	3452	4.79	0.59	0.03	2.44 ± 0.01	2.90	2.61 ± 0.01
J02123+035	BD+02 348	3605	4.90	0.58	−0.35	1.80 ± 0.02	2.57	2.45 ± 0.03
J02222+478	BD+47 612	3916	4.64	0.58	0.15	2.43 ± 0.02	2.95	2.70 ± 0.01
J02358+202	BD+19 381	3726	4.63	0.59	0.18	2.48 ± 0.03	2.93	2.60 ± 0.01
J02442+255	G 36–31	3434	4.83	0.58	0.00	2.12 ± 0.02	2.98	2.63 ± 0.01
J02565+554W	G 174–19	3889	4.64	0.54	0.30	2.54 ± 0.02	2.98	2.73 ± 0.01
J03181+382	BD+37 748	3854	4.64	0.58	0.20	2.72 ± 0.01	3.20	2.83 ± 0.02
J03213+799	GJ 133	3533	4.78	0.59	−0.10	2.05 ± 0.05	...	2.50 ± 0.01
J03217−066	G 77–46	3502	4.85	0.54	−0.10	1.99 ± 0.04	2.98	2.65 ± 0.02
J03463+262	HD 23453	4001	4.66	0.54	0.20	2.40 ± 0.05	3.11	2.78 ± 0.02
J03531+625	Ross 567	3454	4.79	0.59	−0.05	2.00 ± 0.02	2.65	2.48 ± 0.01
J04225+105	LSPM J0422+1031	3415	4.80	...	0.05	2.55 ± 0.01	2.89	2.73
J04290+219	HD 28343	4187	4.63	0.54	0.30	2.65 ± 0.01	3.17	2.85 ± 0.05
J04376−110	BD−11 916	3611	4.74	0.59	0.05	2.12 ± 0.05	2.93	2.70 ± 0.01
J04376+528	HD 232979	4010	4.64	0.58	0.00	2.10 ± 0.05	2.92	2.63 ± 0.01
J04429+189	HD 285968	3689	4.66	0.58	0.12	2.54 ± 0.01	2.85	2.60 ± 0.01
J04538−177	L 736-30	3543	4.76	0.58	−0.10	2.06 ± 0.01	2.60	2.50 ± 0.01
J04588+498	BD+49 1280	4004	4.64	0.52	0.15	2.36 ± 0.03	3.00	2.79 ± 0.04
J05127+196	GJ 192	3570	4.75	0.54	−0.01	2.19 ± 0.02	2.87	2.78 ± 0.02
J05314−036	HD 36395	3700	4.95	0.67	0.25	2.70 ± 0.02	3.40	2.97 ± 0.02
J05365+113	HD 245409	4062	4.66	0.43	0.05	2.24 ± 0.03	3.05	2.79 ± 0.01
J05415+534	HD 233153	3869	4.63	0.63	0.15	2.38 ± 0.02	3.00	2.82 ± 0.02
J06103+821	GJ 226	3500	4.90	0.57	−0.05	2.07 ± 0.02	2.85	2.65 ± 0.05
J06105−218	HD 42581	3842	4.68	0.54	0.10	2.43 ± 0.02	2.90	2.66 ± 0.03
J06371+175	Ross 85	3732	4.77	0.63	−0.25	1.83 ± 0.02	2.40	2.37
J06548+332	Wolf 294	3410	4.85	0.57	0.00	2.28 ± 0.05	2.87	2.62 ± 0.01
J07044+682	GJ 258	3421	4.81	0.57	0.05	2.32 ± 0.01	2.90	2.65 ± 0.01
J07287−032	GJ 1097	3420	4.81	0.58	0.01	2.30 ± 0.02	2.83	2.63 ± 0.02
J07353+548	GJ 3452	3513	4.81	0.59	−0.05	2.08 ± 0.01	2.70	2.63 ± 0.01
J07361−031	BD−02 2198	3790	4.70	...	−0.04	2.05 ± 0.02	2.60	2.59 ± 0.02
J08161+013	G 113–0	3534	4.77	0.57	−0.04	2.15 ± 0.01	2.60	2.60 ± 0.01
J08293+039	2M J08292191+0355092	3685	4.64	0.54	0.22	2.52 ± 0.01	2.88	2.63 ± 0.01
J08358+680	G 234–37	3434	4.82	0.57	−0.06	2.05 ± 0.01	2.85	2.64 ± 0.03
J09133+688	G 234–57	3494	4.86	...	−0.05	2.00 ± 0.05	2.98	2.70 ± 0.05
J09140+196	LP 427–16	3591	4.65	0.58	0.11	2.20 ± 0.05	2.95	2.59 ± 0.01
J09143+526	HD 79210	4007	4.67	0.58	0.07	2.17 ± 0.02	2.97	2.68 ± 0.01
J09144+526	HD 79211	3980	4.67	0.49	0.10	2.17 ± 0.01	2.95	2.71 ± 0.02
J09163−186	L 749–34	3524	4.85	0.57	−0.12	1.97 ± 0.01	2.89	2.72 ± 0.02
J09411+132	Ross 85	3654	4.72	0.57	0.03	2.19 ± 0.02	2.90	2.65 ± 0.01
J09425+700	GJ 360	3718	4.67	0.41	0.10	2.55 ± 0.02	2.80	2.80
J11054+435	BD+44 2051A	3617	4.79	0.43	−0.20	2.05 ± 0.02	2.80	2.53
J11201−104 [(a)]	LP 733–099	3469	4.91	0.58	−0.20	1.78 ± 0.02	2.57	2.50 ± 0.01
J12111−199	LTT 4562	3440	4.83	0.59	−0.10	2.18 ± 0.02	2.75	2.70
J13450+176	BD+18 2776	3900	4.80	0.57	−0.50	1.75 ± 0.05	2.30	2.20
J13457+148	HD 119850	3610	4.73	0.47	−0.10	2.12 ± 0.02	2.58	2.65
J15218+209 [(a)]	OT Ser	3500	4.90	0.58	0.10	2.05	2.71	2.70 ± 0.02
J18174+483 [(a)]	TYC 3529-1437-1	3435	4.80	0.59	−0.08	1.85 ± 0.02	2.88	2.58 ± 0.01
J22565+165	HD 216899	3606	4.77	0.59	0.15	2.55 ± 0.01	3.02	2.75

Notes. The C/O ratio in the Sun is 0.575 (Lodders 2019). Abundances of Rb, Sr, and Zr are given on the scale log N(H) ≡ 12. The Sr abundances shown are corrected for non-LTE effects (see text). For Rb and Zr abundances, the abundance dispersion is also tabulated. [(a)]The resonance Rb lines in these stars may be affected by magnetic field. Their abundance ratios are indicated as red open circles in Figs. 5 and 8.